STEELS

H. K. D. H. BHADESHIA

Question and example class documents attached to the end of this handout.

The book associated with this course: "Steels", 2017, 4th edition, H. K. D. H. Bhadeshia and R. W. K. Honeycombe, available on the Tripos reference shelves in the library.

Many questions associated with this course are on:

https://edge.edx.org/courses/MSM/M21/2013_Winter/about

You may click directly on the above link on your PDF file to reach the location. The link will take you to an automated learning system based on the edX platform courtesy of Harvard and MIT.

In order to optimally benefit from this system, you should attempt one set of questions after each lecture. This will test your understanding of the lecture material. Marking is fully automated. Supervisions can therefore be better exploited to deal with conceptual difficulties and for broadening the discussion.

The full set of resources associated with this course is available on:

http://www.phase-trans/msm.cam.ac.uk/teaching.html

1. Martensite in Steels

The name *martensite* is after the German scientist Martens. It was used originally to describe the hard microconstituent found in quenched steels. Martensite remains of the greatest technological importance in steels where it can confer an outstanding combination of strength ($> 3500\,\mathrm{MPa}$) and toughness ($> 200\,\mathrm{MPa\,m^{\frac{1}{2}}}$). Many materials other than steel are now known to exhibit the same type of solid-state phase transformation, known as a *martensitic transformation*, frequently also called a *shear* or *displacive transformation*. Martensite occurs in, for example, nonferrous alloys, pure metals, ceramics, minerals, inorganic compounds, solidified gases and polymers (Table 1). We shall review first the experimental facts about martensite and then proceed to explain them.

1.1. **Diffusionless Character.** Martensitic transformations are diffusionless, but what evidence is there to support this?

TABLE 1. The temperature M_S at which martensite first forms on cooling, and the approximate Vickers hardness of the resulting martensite for a number of materials.

Composition	M_S / K	Hardness HV
ZrO_2	1200	1000
Fe–31Ni–0.23C wt%	83	300
Fe–34Ni–0.22C wt%	< 4	250
Fe–3Mn–2Si–0.4C wt%	493	600
Cu–15Al	253	200
Ar–$40N_2$	30	

Martensite can form at very low temperatures, where diffusion, even of interstitial atoms, is not conceivable over the time period of the experiment. Table 1 gives values of the highest temperature at which martensite forms in a variety of materials; this temperature is known as the martensite–start, or M_S temperature. It is obvious that although martensite *can* form at low temperatures, it need not do so. Therefore, a low transformation temperature is not sufficient evidence for diffusionless transformation.

Martensite plates can grow at speeds which approach that of sound in the metal. In steel this can be as high as $1100\,\mathrm{m\,s^{-1}}$, which compares with the fastest recorded solidification front velocity of about $80\,\mathrm{m\,s^{-1}}$ in pure nickel. Such large speeds are inconsistent with diffusion during transformation. Note that martensite need not grow so rapidly. For example, in shape–memory alloys or in single–interface transformations, the interface velocity is small enough to observe.

The chemical composition of martensite can be measured and shown to be identical to that of the parent austenite. The totality of these observations demonstrate convincingly that martensitic transformations are diffusionless.

1.2. **The Habit Plane.** This is the interface plane between austenite and martensite as measured on a macroscopic scale (Fig. 1), for example by using one or two–surface crystallographic trace analysis on metallographic samples. For unconstrained transformations this interface plane is flat, but strain energy minimisation introduces some curvature when the transformation is constrained by its surroundings. Nevertheless, the macroscopic habit plane is identical for both cases, as illustrated in Fig. 1.

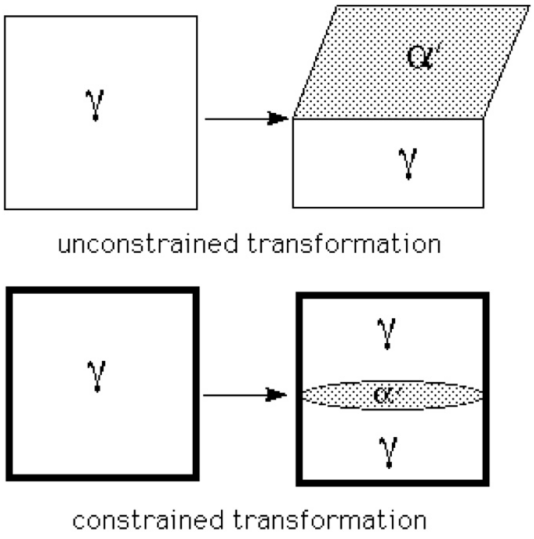

FIGURE 1. An illustration of the habit plane between austenite (γ) and martensite (α').

Steels of vastly different chemical composition can have martensite with the same habit plane (Table 2), and indeed, other identical crystallographic characteristics.

TABLE 2. Habit plane indices for martensite. With the exception of ϵ–martensite, the quoted indices are approximate because the habit planes are in general irrational.

Composition /wt.%	Approximate habit plane indices
Low–alloy steels, Fe–28Ni	$\{1\ 1\ 1\}_\gamma$
Plate martensite in Fe–1.8C	$\{2\ 9\ 5\}_\gamma$
Fe–30Ni–0.3C	$\{3\ 15\ 10\}_\gamma$
Fe–8Cr–1C	$\{2\ 5\ 2\}_\gamma$
ϵ–martensite in 18/8 stainless steel	$\{1\ 1\ 1\}_\gamma$

1.3. **Orientation Relationships.** The formation of martensite involves the coordinated movement of atoms. It follows that the austenite and martensite lattices will be intimately related. All martensitic transformations therefore lead to a reproducible orientation relationship between the parent and product lattices. It is frequently the

case that a pair of corresponding close–packed[1] planes in the ferrite and austenite are parallel or nearly parallel, and it is usually the case that corresponding directions within these planes are roughly parallel:

Kurdjumov–Sachs

$$\begin{array}{rcl} \{1\ 1\ 1\}_\gamma & || & \{0\ 1\ 1\}_\alpha \\ \langle 1\ 0\ \overline{1}\rangle_\gamma & || & \langle 1\ 1\ \overline{1}\rangle_\alpha \end{array}$$

Nishiyama–Wasserman

$$\begin{array}{rcl} \{1\ 1\ 1\}_\gamma & || & \{0\ 1\ 1\}_\alpha \\ \langle 1\ 0\ \overline{1}\rangle_\gamma \text{ about } 5.3^\circ \text{ from} & & \langle 1\ 1\ \overline{1}\rangle_\alpha \text{ towards } \langle \overline{1}\ 1\ \overline{1}\rangle_\alpha \end{array}$$

Greninger–Troiano

$$\begin{array}{rl} \{1\ 1\ 1\}_\gamma \text{ about } 0.2^\circ \text{ from} & \{0\ 1\ 1\}_\alpha \\ \langle 1\ 0\ \overline{1}\rangle_\gamma \text{ about } 2.7^\circ \text{ from} & \langle 1\ 1\ \overline{1}\rangle_\alpha \text{ towards } \langle \overline{1}\ 1\ \overline{1}\rangle_\alpha \end{array}$$

Note that these have been stated approximately: the true relations are irrational, meaning that the indices of the parallel planes and directions cannot be expressed using rational numbers (the square root of 2 is not a rational number).

1.4. **Athermal Nature of Transformation.** In the vast majority of cases, the extent of reaction is found to be virtually independent of time:

$$1 - V_{\alpha'} = \exp\{\beta(M_S - T)\} \qquad \text{where} \qquad \beta \simeq -0.011 \tag{1}$$

$V_{\alpha'}$ is the fraction of martensite and T is a temperature below M_S. This is the Koistinen and Marburger equation; notice that time does not feature in this relation, so that the fraction of martensite depends only on the undercooling below the martensite–start temperature. This athermal character is a consequence of very rapid nucleation and growth, so rapid that the time taken can in normal circumstances be neglected.

[1]The body–centred cubic lattice does not have a close–packed plane but $\{0\ 1\ 1\}_\alpha$ is the most densely packed plane.

Isothermal martensite *is* possible when nucleation is hindered, although the growth rate of individual plates of martensite can still be rapid.

1.5. **Structure of the Interface.** Any process which contributes to the formation of martensite cannot rely on assistance from thermal activation. There must therefore exist a high level of continuity across the interface, which must be coherent or semi-coherent. A stress–free fully coherent interface is impossible for the $\gamma \rightarrow \alpha'$ transformation since the lattice deformation **BR** is an invariant–line strain. A semi–coherent interface must be such that the interfacial dislocations can glide as the interface moves (climb is not permitted). It follows that the Burgers vectors of the interface dislocations must not lie in the interface plane unless the dislocations are screw in character.

There is an additional condition for a semi–coherent interface to be glissile. The line vectors of the interfacial dislocations must lie along an *invariant–line*, *i.e.* a line which joins the parent and product crystals without any rotation or distortion. Why is that? If there is any distortion along the dislocation line, then other dislocations are needed to accommodate that misfit. It will then be necessary to have more than one set of non–parallel dislocations in the interface. These non–parallel dislocations can intersect to form jogs which render the interface sessile.

It follows that for martensitic transformation to be possible, the deformation which changes the parent into the product must leave one or more lines invariant (unrotated, undistorted). A deformation which leaves one line invariant is called an 'invariant–line strain'.

1.6. **The Shape Deformation.** The passage of a slip dislocation through a crystal causes the formation of a step where the glide plane intersects the free surface (Fig. 2a,b). The passage of many such dislocations on parallel slip planes causes macroscopic shear (Fig. 2c,d). Slip causes a change in shape but not a change in the crystal structure, because the Burgers vectors of the dislocations are also lattice vectors.

During martensitic transformation, the pattern in which the atoms in the parent crystal are arranged is *deformed* into that appropriate for martensite, there must be a corresponding change in the macroscopic shape of the crystal undergoing transformation. The dislocations responsible for the deformation are in the α'/γ interface, with Burgers vectors such that in addition to deformation they also cause the change in crystal structure. The deformation is such that an initially flat surface becomes uniformly tilted about the line formed by the intersection of the interface plane with the free surface. Any scratch traversing the transformed region is similarly deflected though the scratch remains connected at the α'/γ interface. These observations, and

others, confirm that the measured shape deformation is an invariant–plane strain (Fig. 2e–g) with a large shear component ($\simeq 0.22$) and a small dilatational strain ($\simeq 0.03$) directed normal to the habit plane.

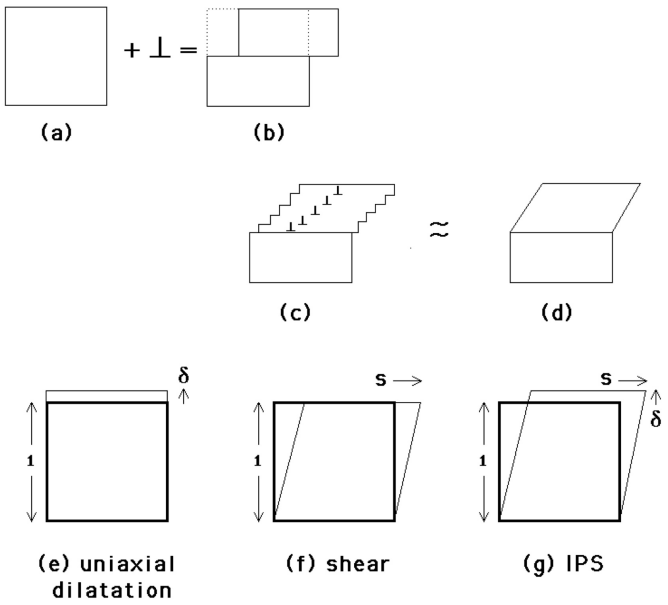

FIGURE 2. (a, b) Step caused by the passage of a slip dislocation. (c, d) Many slip dislocations, causing a macroscopic shear. (e) An invariant–plane strain with a uniaxial dilatation. (f) An invariant–plane strain which is a simple shear. (g) An invariant–plane strain which is the combined effect of a uniaxial dilatation and a simple shear.

1.7. **Bain Strain.** We now consider the nature of the strain necessary to transform the c.c.p. lattice of γ into the b.c.c. lattice of α'. Such a strain was proposed by Bain in 1924 and hence is known as the 'Bain Strain' (Fig. 3). There is a compression along the z axis and a uniform expansion along the x and y axes.

The deformation describing the Bain Strain is given by

$$\mathbf{B} = \begin{pmatrix} \epsilon_0 & 0 & 0 \\ 0 & \epsilon_0 & 0 \\ 0 & 0 & \epsilon_0' \end{pmatrix} \tag{2}$$

$$\epsilon_0 = \frac{\sqrt{2}a_{\alpha'} - a_\gamma}{a_\gamma} \qquad \epsilon_0' = \frac{a_{\alpha'} - a_\gamma}{a_\gamma} \tag{3}$$

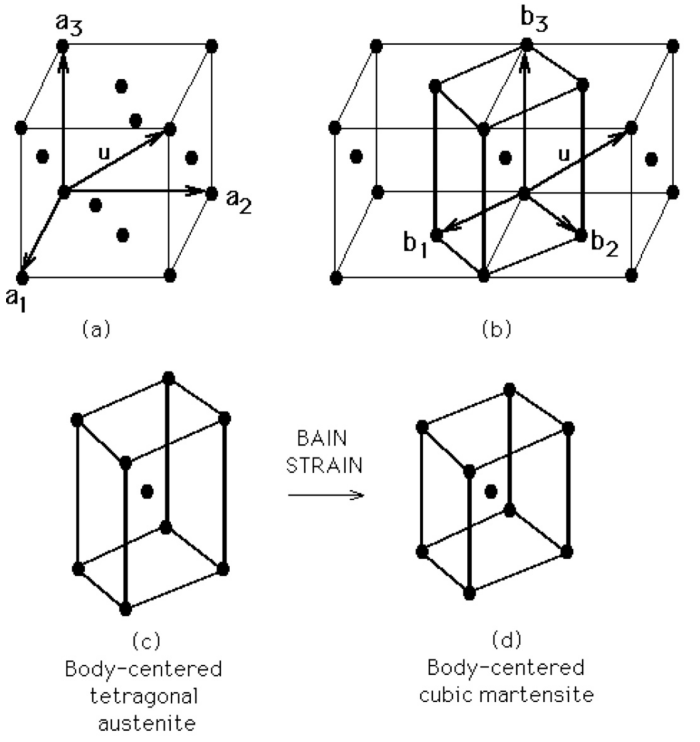

FIGURE 3. The Bain strain (not all lattice points illustrated).

where $a_{\alpha'}$ and a_γ are the lattice parameters of martensite and austenite respectively. The contraction is therefore along the $[0\ 0\ 1]_\gamma$ axis and a uniform expansion on the $(0\ 0\ 1)_\gamma$ plane.

The Bain strain implies the following orientation relationship between the parent and product lattices:

$$[0\ 0\ 1]_{fcc}||[0\ 0\ 1]_{bcc} \qquad [1\ \overline{1}\ 0]_{fcc}||[1\ 0\ 0]_{bcc} \qquad [1\ 1\ 0]_{fcc}||[0\ 1\ 0]_{bcc}$$

but in fact, the experimentally observed orientation relationships are irrational, as discussed earlier. We shall deal with this inconsistency later.

Temporarily neglecting the fact that the Bain orientation is inconsistent with experiments, we proceed to examine whether the Bain strain leaves at least one line invariant. After all, this is a necessary condition for martensitic transformation.

In Fig. 4a,b, the austenite is represented as a sphere which, as a result of the Bain strain $\mathbf{B}$, is deformed into an ellipsoid of revolution which represents the martensite. There are no lines which are left undistorted or unrotated by $\mathbf{B}$. There are no lines in the $(0\ 0\ 1)_{fcc}$ plane which are undistorted. The lines wx and yz are undistorted but are rotated to the new positions $w'x'$ and $y'z'$. Such rotated lines

are not invariant. However, the combined effect of the Bain strain **B** and the rigid body rotation **R** is indeed an invariant–line strain (ILS) because it brings yz and $y'z'$ into coincidence (Fig. 4c). This is the reason why the observed irrational orientation relationship differs from that implied by the Bain strain. The rotation required to convert **B** into an ILS precisely corrects the Bain orientation into that which is observed experimentally.

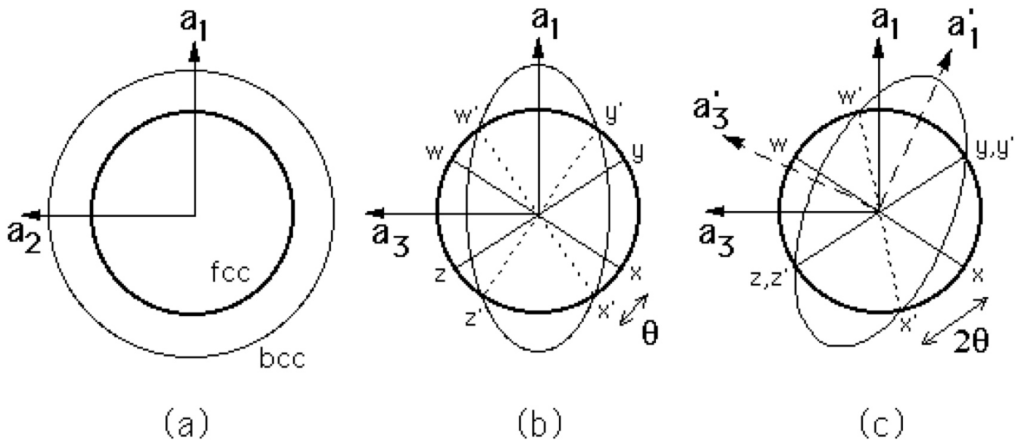

FIGURE 4. (a) and (b) show the effect of the Bain strain on austenite, which when undeformed is represented as a sphere of diameter $wx = yz$ in three–dimensions. The strain transforms it to an ellipsoid of revolution. (c) shows the invariant–line strain obtained by combining the Bain strain with a rigid body rotation through an angle θ.

As can be seen from Fig. 4c, there is no rotation which can make **B** into an invariant–plane strain since this would require two non–parallel invariant–lines. Thus, for the $fcc \rightarrow bcc$ transformation, austenite cannot be transformed into martensite by a homogeneous strain which is an IPS. And yet, the observed shape deformation leaves the habit plane undistorted and unrotated, *i.e.* it is an invariant–plane strain.

The phenomenological theory of martensite crystallography solves this remaining problem (Fig. 5). The Bain strain converts the structure of the parent phase into that of the product phase. When combined with an appropriate rigid body rotation, the net homogeneous lattice deformation **RB** is an invariant–line strain (step a to c in Fig. 5). However, the observed shape deformation is an invariant–plane strain $\mathbf{P_1}$ (step a to b in Fig. 5, but this gives the wrong crystal structure. If a second homogeneous shear $\mathbf{P_2}$ is combined with $\mathbf{P_1}$ (step b to c), then the correct structure

is obtained but the wrong shape since

$$\mathbf{P_1 P_2 = RB}$$

These discrepancies are all resolved if the shape changing effect of $\mathbf{P_2}$ is cancelled macroscopically by an inhomogeneous lattice–invariant deformation, which may be slip or twinning as illustrated in Fig. 5.

The theory explains all the observed features of the martensite crystallography. The orientation relationship is predicted by deducing the rotation needed to change the Bain strain into an invariant–line strain. The habit plane does not have rational indices because the amount of lattice–invariant deformation needed to recover the correct the macroscopic shape is not usually rational. The theory predicts a substructure in plates of martensite (either twins or slip steps) as is observed experimentally. The transformation goes to all the trouble of ensuring that the shape deformation is macroscopically an invariant–plane strain because this reduces the strain energy when compared with the case where the shape deformation might be an invariant–line strain.

1.8. **Thermodynamics of Martensitic Transformations.** Martensite is not represented on phase diagrams because the latter deal with equilibrium. Martensite deviates from equilibrium in two important ways:

Martensite grows without diffusion, so it inherits the chemical composition of the parent austenite. In an equilibrium transformation the chemical elements partition into the parent and product phases in a manner which leads to a minimisation of free energy.

Secondly, the shape deformation associated with martensitic transformation causes strains; the resulting strain energy has to be accounted for before the transformation can happen.

These deviations can be represented on a free energy plot as illustrated in Fig. 6.

TABLE 3. Typical energies associated with martensitic transformation.

	$\mathrm{J\,mol^{-1}}$
Strain energy	600
Twin interface energy	100
γ/α' interface energy	1
Stored energy due to dislocations	20

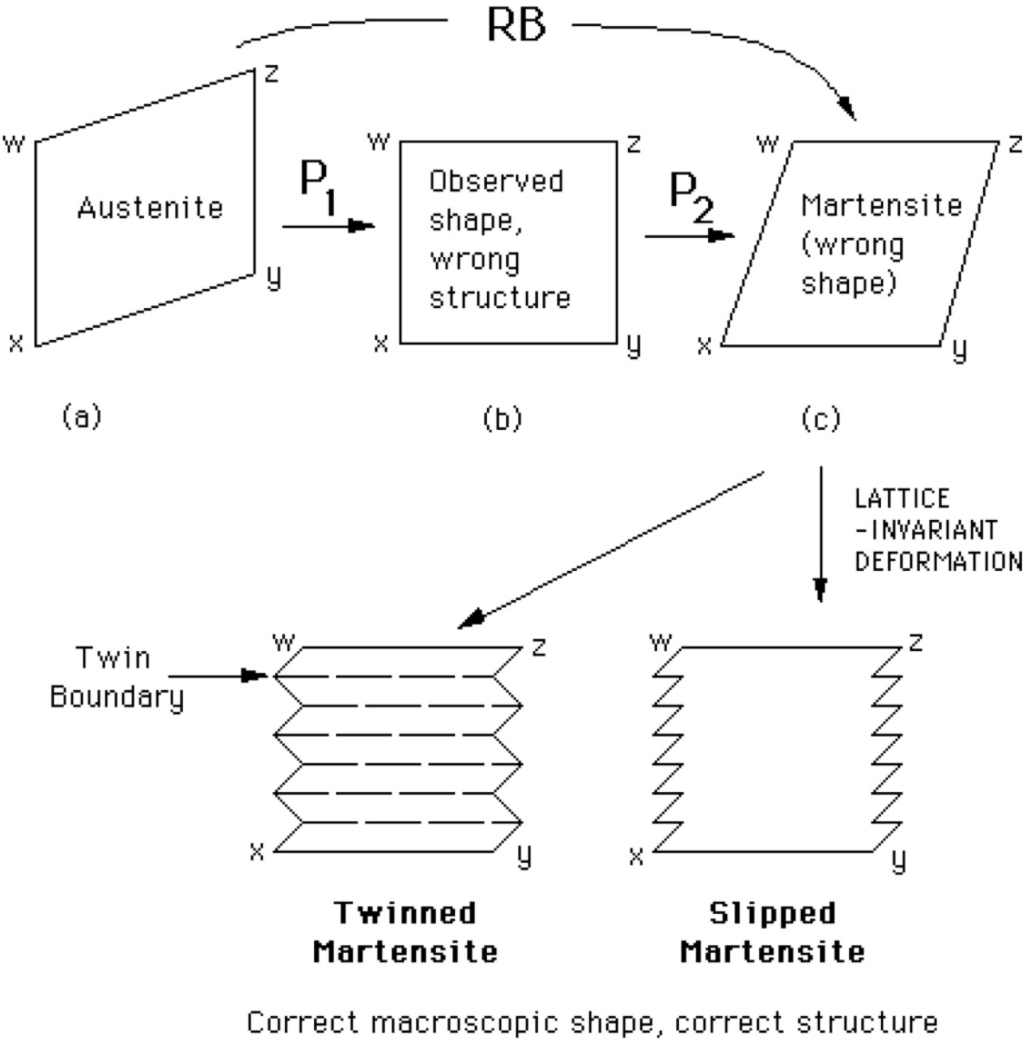

FIGURE 5. The phenomenological theory of martensite crystallography.

The relationship with the phase diagram is illustrated in Fig. 7. Martensitic transformation is only possible below the T_0' temperature.

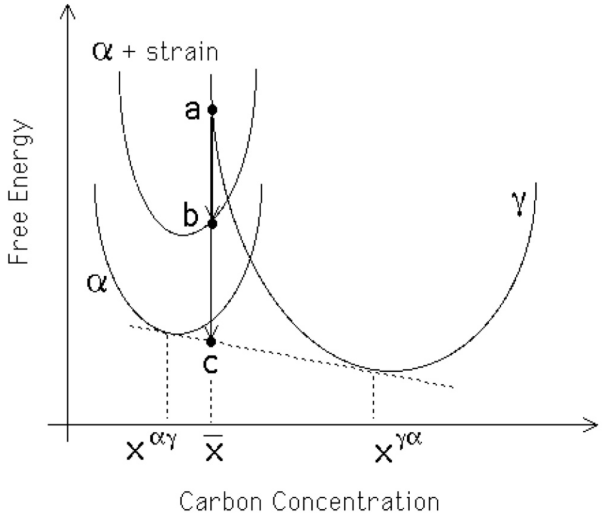

FIGURE 6. The distance **ac** represents the free energy decrease when austenite of composition $\overline{x}$ decomposes into an equilibrium mixture of ferrite and austenite of compositions $x^{\alpha\gamma}$ and $x^{\gamma\alpha}$ respectively. The distance **ab** is the smaller decrease in free energy when martensite forms without any composition change, taking into account the strain associated with the transformation.

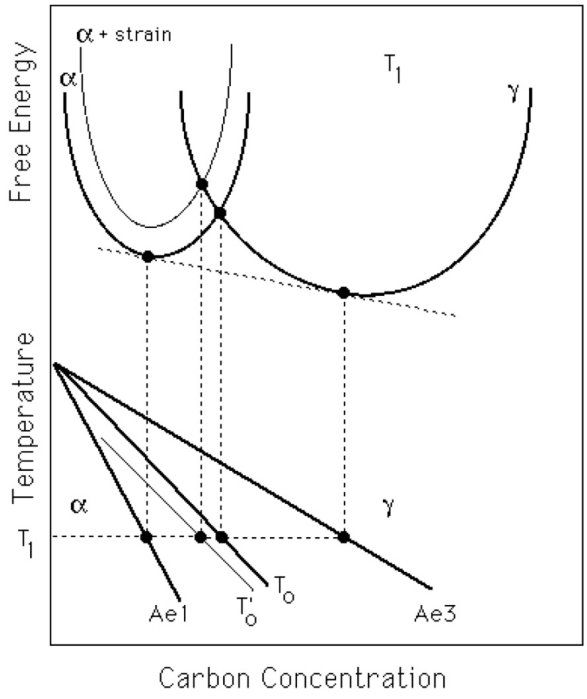

FIGURE 7. Schematic illustration of the origin of the T_0 curve on the phase diagram. The T_0' curve incorporates a strain energy term for the ferrite, illustrated on the diagram by raising the free energy curve for ferrite by an appropriate quantity.

2. Bainite in Steels

Bainite forms by the decomposition of austenite at a temperature which is above M_S but below that at which fine pearlite forms. All bainite forms below the T_0 temperature.

All time–temperature–transformation (TTT) diagrams consist essentially of two C–curves (Fig. 8). If we focus first on the Fe–Mn–C steel with the higher hardenability (slower rates of transformation) then the two curves are separated. The upper C–curve represents the time required to initiate reconstructive transformations such as ferrite or pearlite, whereas the lower C–curve represents displacive transformations such as bainite or Widmanstätten ferrite. Notice that as the hardenability of the steel decreases, the two curves tend to overlap so that in experiments it appears as if the TTT diagram contains just one curve with a complicated shape, describing all the reactions. This is not the case because it is possible to show that this is an experimental artefact caused by the inability to detect the two C–curves separately.

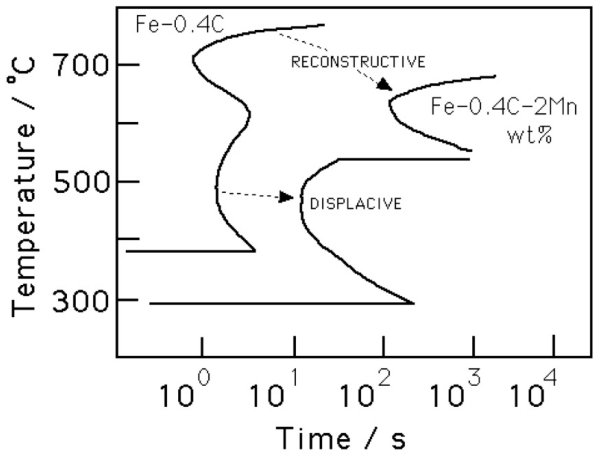

Figure 8. TTT diagrams for two steels, one of which has a high hardenability.

A further feature to note (Fig. 8, Fe–Mn–C) is that the lower C–curve representing displacive transformations has a flat top. This represents the highest temperature T_h at which displacive transformations may occur. The temperature T_h may equal the bainite–start temperature B_S if the hardenability is high enough, but otherwise, $T_h = W_S$ where W_S is the Widmanstätten ferrite start–temperature (Fig. 9). The latter does not form in high–hardenability steels and we shall discuss in this lecture the detailed differences between bainite and Widmanstätten ferrite.

Bainite is a non–lamellar aggregate of carbides and plate–shaped ferrite (Fig. 10). As we shall see later, the carbide part of the microstructure is not essential; the carbides form as a secondary reaction, rather as in the tempering of martensite. The ferrite

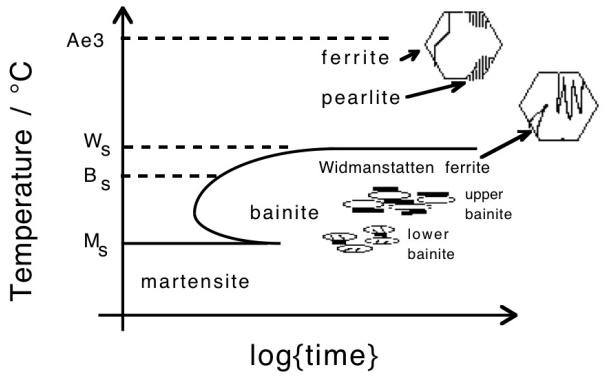

FIGURE 9. TTT diagrams showing the different domains of transformation.

plates are each about 10μm long and about 0.2μm thick, making the individual plates invisible in the optical microscope.

Upper bainite consists of clusters of platelets of ferrite adjacent to each other and in almost identical crystallographic orientation, so that a low–angle boundary arises whenever the adjacent platelets touch. The ferrite always has a Kurdjumov–Sachs type orientation relationship with the austenite in which it grows.

Elongated cementite particles usually decorate the boundaries of these platelets, the amount and continuity of the cementite layers depending on the carbon concentration of the steel.

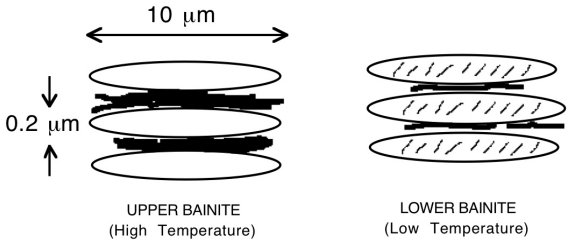

FIGURE 10. Schematic illustration of the microstructure of upper and lower bainite.

The clusters of ferrite plates are known as 'sheaves' (Fig. 11); each sheaf is itself in the form of a wedge–shaped plate on a macroscopic scale. The sheaves inevitably nucleate heterogeneously at austenite grain surfaces. The cementite precipitates from the carbon–enriched austenite between the ferrite plates; the ferrite itself is free from carbides. Cementite precipitation from austenite can be prevented by increasing the silicon concentration to about 1.5 wt%; this works because silicon is insoluble in cementite. Silicon–rich bainitic steels can have very good toughness because of the absence of brittle cementite.

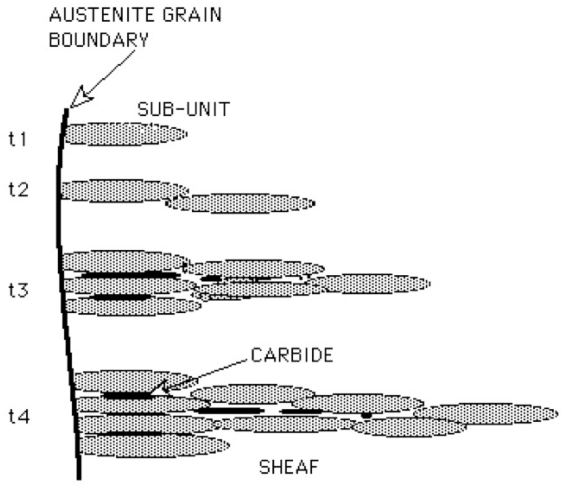

FIGURE 11. Evolution of a bainite sheaf as a function of time.

2.1. **Shape Deformation.** The formation of bainite causes a deformation (Fig. 12) which is an invariant–plane strain with a shear component of about 0.26 and a dilatational strain normal to the habit plane of about 0.03. This is consistent with a displacive mechanism of transformation.

Bainite forms at a relatively high temperature when compared with martensite. The parent austenite is weaker at high temperatures and cannot accommodate the large shape deformation elastically. It therefore relaxes by plastic deformation in the region adjacent to the bainite. This is evident in Fig. 12, but is also presented as a height scan in Fig. 13. The effect of this plastic deformation is to stifle the growth of bainite plates before they hit any obstacle. This is why each bainite plate grows to a size which is often smaller than the austenite grain size and then comes to a halt. Further transformation happens by the formation of a new plate and this is why the sheaf morphology arises.

2.2. **Substitutional Alloying Elements.** These do not redistribute at all during transformation, even though equilibrium requires them to partition between the austenite and ferrite (Fig. 14). The ratio of substitutional to iron atoms remains constant everywhere including across the interface. This is consistent with a displacive mechanism of transformation and the existence of an atomic correspondence between the austenite and bainitic ferrite. The results exclude any mechanism which involves local equilibrium at the interface, or solute drag effects associated with interfacial motion.

2.3. **Interstitial Alloying Elements (C, N)).** It appears from Fig. 14 that the carbon has partitioned into the austenite. It is simple to establish that martensitic

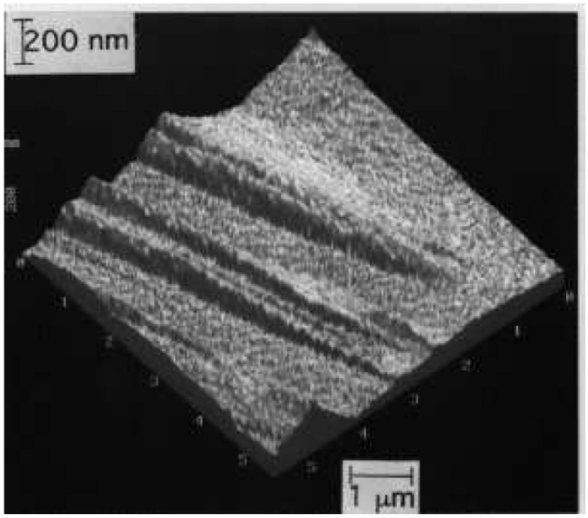

FIGURE 12. Atomic force microscope image of the displacements caused on a polished surface of austenite by the growth of bainite. Notice the shear deformation (dark contrast) and indeed the plastic accommodation (light contrast tapering from the ridge of the region of dark contrast) of the shape change in the austenite adjacent to the bainite plates.

transformation is diffusionless, by measuring the local compositions before and after transformation. Bainite forms at somewhat higher temperatures where the carbon can escape out of the plate within a fraction of a second. Its original composition cannot therefore be measured directly.

There are three possibilities. The carbon may partition during growth so that the ferrite may never contain any excess carbon. The growth may on the other hand be diffusionless with carbon being trapped by the advancing interface. Finally, there is an intermediate case in which some carbon may diffuse with the remainder being trapped to leave the ferrite partially supersaturated. It is therefore much more difficult to determine the precise role of carbon during the growth of bainitic ferrite than in martensite.

Diffusionless growth requires that transformation occurs at a temperature below T_0, when the free energy of bainite becomes less than that of austenite of the same composition. A locus of the T_0 temperature as a function of the carbon concentration is called the T_0 curve, an example of which is plotted on the Fe–C phase diagram in

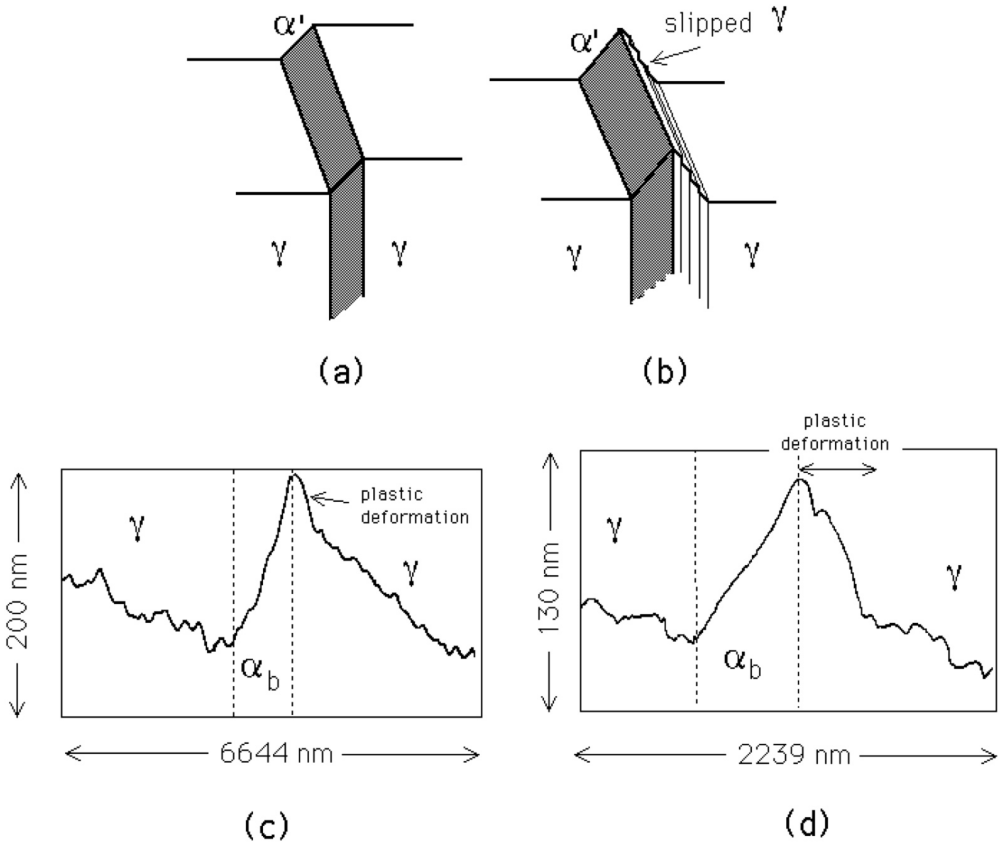

FIGURE 13. (a) A perfect invariant–plane strain surface relief effect. (b) One where plastic relaxation of the shape change occurs in the adjacent matrix. (c,d) An actual atomic force microscope scan across the surface relief due to a bainite sub–unit (Swallow and Bhadeshia, 1996).

Fig. 15. Growth without diffusion can only occur if the carbon concentration of the austenite lies to the left of the T_0 curve.

Suppose that the plate of bainite forms without diffusion, but that any excess carbon is soon afterwards rejected into the residual austenite. The next plate of bainite then has to grow from carbon–enriched austenite (Fig. 16 a). This process must cease when the austenite carbon concentration reaches the T_0 curve. The reaction is said to be incomplete, since the austenite has not achieved its equilibrium composition (given by the Ae3 curve) at the point the reaction stops. If on the other hand,

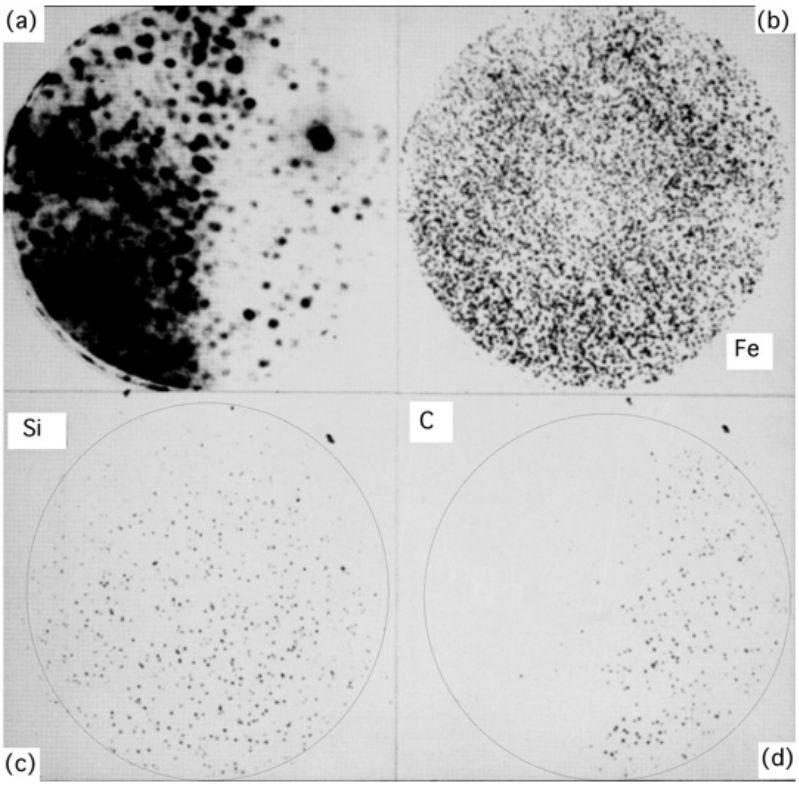

FIGURE 14. Imaging atom–probe micrographs, taken across an austenite–bainitic ferrite interface in a Fe–C–Si–Mn alloy. The images confirm quantitative data (Bhadeshia and Waugh, 1982) showing the absence of any substitutional atom diffusion during transformation. (a) Field–ion image; (b) corresponding silicon map; (c) corresponding carbon map; (d) corresponding iron map.

the ferrite grows with an equilibrium carbon concentration then the transformation should cease when the austenite carbon concentration reaches the Ae3 curve.

It is found experimentally that the transformation to bainite does indeed stop at the T_0 boundary (Fig. 16 b). The balance of the evidence is that the growth of bainite below the B_S temperature involves the successive nucleation and martensitic growth of sub–units, followed in upper bainite by the diffusion of carbon into the surrounding austenite. The possibility that a small fraction of the carbon is nevertheless partitioned during growth cannot entirely be ruled out, but there is little doubt that the bainite is at first substantially supersaturated with carbon.

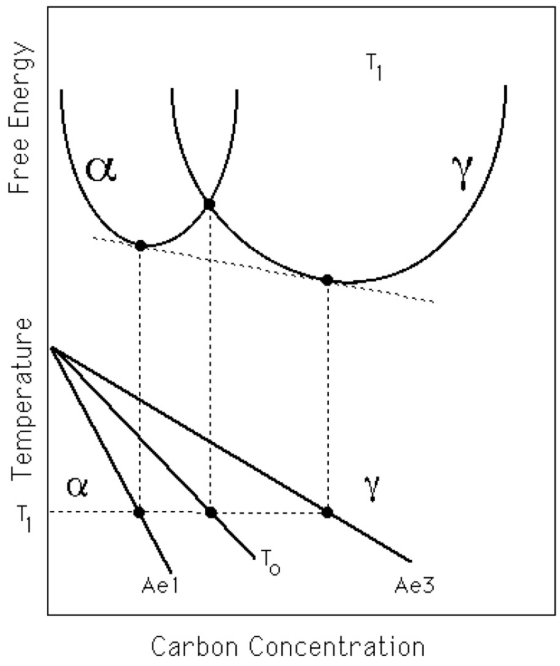

FIGURE 15. Schematic illustration of the origin of the T_0 construction on the Fe–C phase diagram. Austenite with a carbon concentration to the left of the T_0 boundary can in principle transform without any diffusion. Diffusionless transformation is thermodynamically impossible if the carbon concentration of the austenite exceeds the T_0 curve.

These conclusions are not significantly modified when the strain energy of transformation is included in the analysis.

There are two important features of bainite which can be shown by a variety of techniques, *e.g.* dilatometry, electrical resistivity, magnetic measurements and by metallography. Firstly, there is a well defined temperature B_S above which no bainite will form, which has been confirmed for a wide range of alloy steels. The amount of bainite that forms increases as the transformation temperature is reduced below the B_S temperature. The fraction increases during isothermal transformation as a sigmoidal function of time, reaching an asymptotic limit which does not change on prolonged heat treatment even when substantial quantities of austenite remain untransformed. Transformation in fact ceases before the austenite achieves its equilibrium composition, so that the effect is dubbed the "incomplete–reaction phenomenon".

These observations are understood when it is realised that growth must cease if the carbon concentration in the austenite reaches the T_0 curve of the phase diagram.

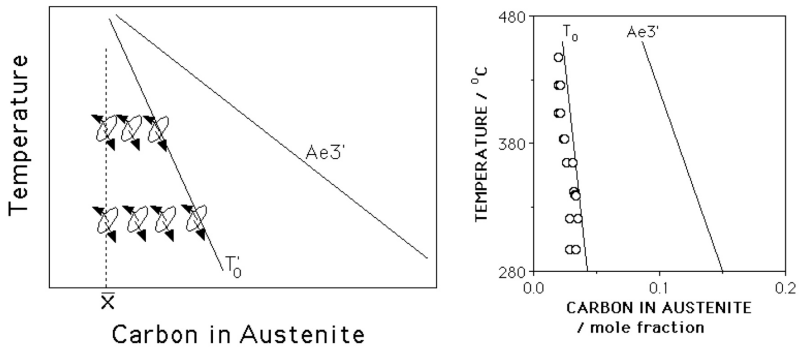

FIGURE 16. (a) Illustration of the incomplete reaction phenomenon. During isothermal transformation, a plate of bainite grows without diffusion, then partitions its excess carbon into the residual austenite. The next plate therefore has to grow from carbon–enriched austenite. This process continues until diffusionless transformation becomes impossible when the austenite composition eventually reaches the T_0 boundary. (b) Experimental data showing that the growth of bainite stops when the austenite carbon concentration reaches the T_0 curve (Fe–0.43C–3Mn–2.12Si wt.% alloy).

Since this condition is met at ever increasing carbon concentrations when the transformation temperature is reduced, more bainite can form with greater undercoolings below B_S. But the T_0 restriction means that equilibrium, when the austenite has a composition given by the Ae3 phase boundary, can never be reached, as observed experimentally. A bainite–finish temperature B_F is sometimes defined, but this clearly cannot have any fundamental significance.

2.4. **Summary.** Bainite grows by displacive transformation; the growth is accompanied by a shape deformation which is an invariant–plane strain with a large shear component. The transformation is diffusionless but carbon atoms partition into the residual austenite (or precipitate as carbides), shortly after growth is arrested. The precipitation of carbides is therefore a secondary event.

3. Alloy design: strong bainite

High-strength bainitic steels have not in practice been as successful as quenched and tempered martensitic steels, because the coarse cementite particles in bainite are detrimental for toughness. However, it is now known that the precipitation of cementite during bainitic transformation can be suppressed. This is done by alloying the steel with about 1.5 wt% of silicon, which has a very low solubility in cementite and greatly retards its growth.

An interesting microstructure results when this silicon-alloyed steel is transformed into upper bainite. The carbon that is rejected into the residual austenite, instead of precipitating as cementite, remains in the austenite and stabilises it down to ambient temperature. The resulting microstructure consists of fine plates of bainitic ferrite separated by carbon-enriched regions of austenite (Fig. 17).

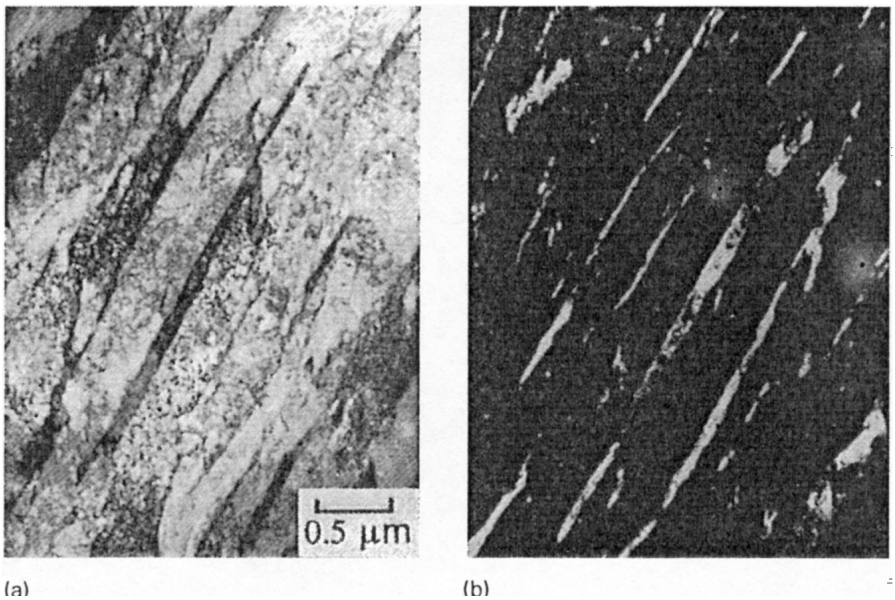

Figure 17. Transmission electron micrograph of a mixture of bainitic ferrite and stable austenite. (a) Bright field image. (b) Retained austenite dark field image.

The potential advantages of the mixed microstructure of bainitic ferrite and austenite can be listed as follows:

1. Cementite is responsible for initiating fracture in high-strength steels. Its absence is expected to make the microstructure more resistant to cleavage failure and void formation.

2. The bainitic ferrite is almost free of carbon, which is known to embrittle ferritic microstructures.

3. The microstructure derives its strength from the ultrafine grain size of the ferrite plates, which are less than $1\,\mu$m in thickness. It is the thickness of these plates which determines the mean free slip distance, so that the effective grain size is less than a micrometer. This cannot be achieved by any other commercially viable process. It should be borne in mind that grain refinement is the only method available for simultaneously improving the strength and toughness of steels.

4. The ductile films of austenite which are intimately dispersed between the plates of ferrite have a crack blunting effect. They further add to toughness by increasing the work of fracture as the austenite is induced to transform to martensite under the influence of the stress field of a propagating crack. This is the TRIP, or transformation-induced plasticity effect.

5. The diffusion of hydrogen in austenite is slower than in ferrite. The presence of austenite can, therefore, improve the stress corrosion resistance of the microstructure.

6. Steels with the bainitic ferrite and austenite microstructure can be obtained without the use of any expensive alloying additions. All that is required is that the silicon concentration should be large enough to suppress cementite.

In spite of these appealing features, the bainitic ferrite/austenite microstructure does not always give the expected good combination of strength and tough-ness. This is because the relatively large 'blocky' regions of austenite between the sheaves of bainite (Fig. 18) readily transform into high-carbon martensite under the influence of stress. This untempered, hard martensite embrittles the steel.

The blocks of austenite are detrimental to toughness, and anything that can be done to reduce their fraction, or increase their stability to martensitic transformation, would be beneficial. Both of these effects are controlled by the T_0' curve of the phase diagram. This curve determines the composition of the austenite at the point where the reaction to bainite stops. By displacing the curve to larger carbon concentrations, both the fraction of bainite that can form, and the carbon concentration of the residual austenite can be increased. Modifications to the T_0' curve can be achieved by altering the alloy composition. It is therefore necessary to calculate the effect of substitutional solutes on the T_0' curve.

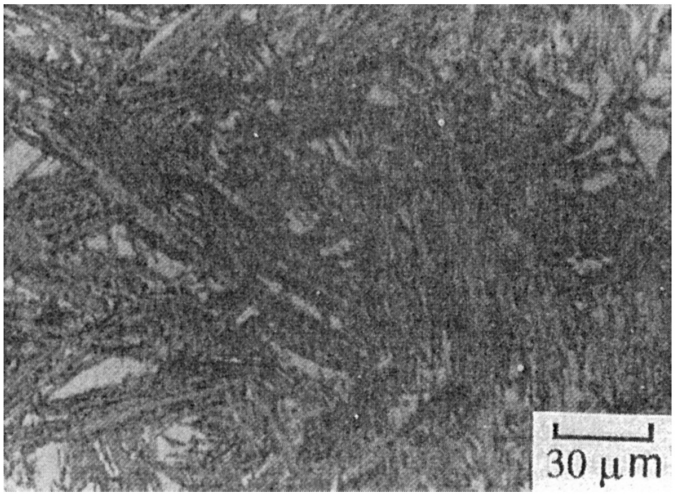

FIGURE 18. Optical micrograph of upper bainite in an Fe–0.43C–3Mn–2.02Si wt% showing the blocks of retained austenite between sheaves of bainite.

3.1. **The improvement in toughness.** An apparently ideal microstructure consisting of bainitic ferrite and ductile austenite in a Fe–3Mn–2.02Si–0.43C wt% exhibits poor toughness because of the presence of blocky unstable austenite (Fig. 19). It is necessary to increase the amount of bainitic ferrite in the microstructure and to increase the stability of the austenite. Both of these aims can be achieved by changing the substitutional solute concentration such that the T_0' curve is shifted to higher carbon concentrations (*i.e.* T_0' is raised at any given carbon concentration).

Manganese has a large effect in depressing the T_0' temperature. An examination of thermodynamic data shows that one possibility is to replace all of the manganese with nickel (Fig. 19). Thus, for a Fe–4Ni–2Si–0.4C wt% (3.69Ni, 3.85Si at%) alloy remarkable improvement in toughness achieved by doing this, without any sacrifice of strength, is illustrated in Fig. 19, along with the T_0' curves as calculated above.

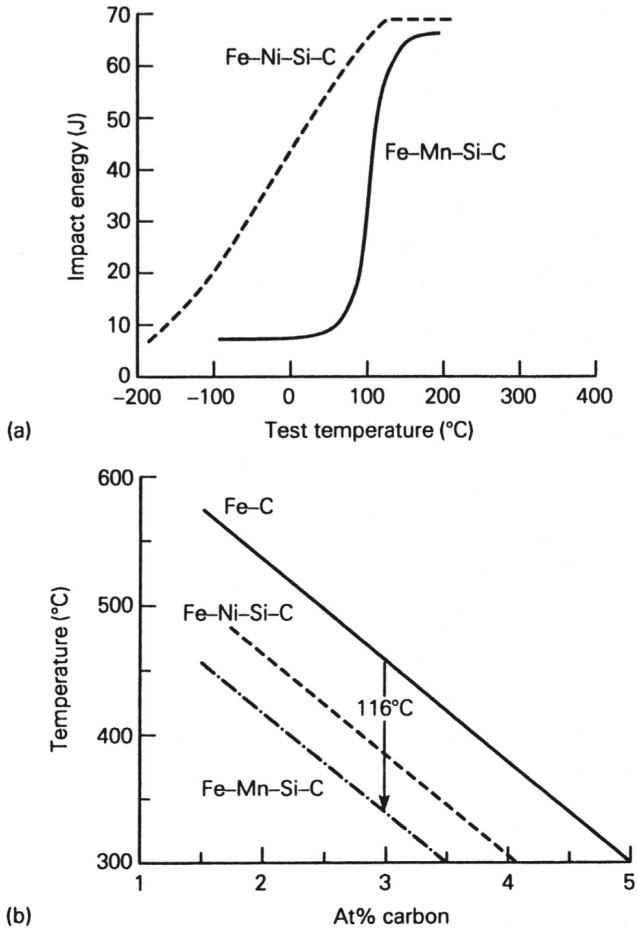

FIGURE 19. (a) Experimentally determined impact transition curves showing how the toughness improves as the amount of blocky austenite is reduced. (b) Calculated T_0' curves for the Fe–C, Fe–Mn–Si–C and Fe–Ni–Si–C steels.

4. Widmanstätten Ferrite

4.1. **Morphology.** Primary Widmanstätten ferrite grows directly from the austenite grain surfaces, whereas secondary Widmanstätten ferrite develops from any allotriomorphic ferrite that may be present in the microstructure (Fig. 20). Widmanstätten ferrite can form at temperatures close to the Ae_3 temperature and hence can occur at very low driving forces; the undercooling needed amounts to a free energy change of only $50\,\mathrm{J\,mol^{-1}}$. This is much less than required to sustain diffusionless transformation.

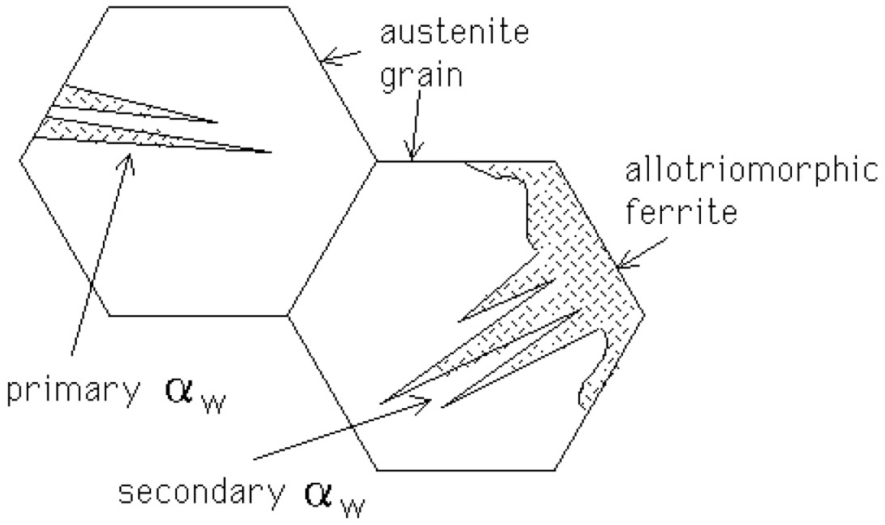

Figure 20. Morphology of primary and secondary Widmanstätten ferrite.

4.2. **Shape Change.** The growth of a single plate of martensite is accompanied by an invariant–plane strain of the type illustrated in Fig. 21a. However, at the high temperatures (low undercoolings) at which Widmanstätten ferrite grows, the driving force is not sufficient to support the strain energy associated with a single plate. Widmanstätten ferrite formation therefore involves the simultaneous and adjacent cooperative growth of two plates, which are crystallographic variants such that their shape deformations mutually accommodate (Fig. 21b). This has the effect of cancelling much of the strain energy.

It follows that what is seen as a single plate in an optical microscope is actually a combination of two variants, usually separated by a low–misorientation boundary (Fig. 21c). Widmanstätten ferrite has a habit plane which is close to $\{5\ 5\ 8\}_\gamma$. Hence, the two plates α_{w1} and α_{w2} which have different variants of this habit with

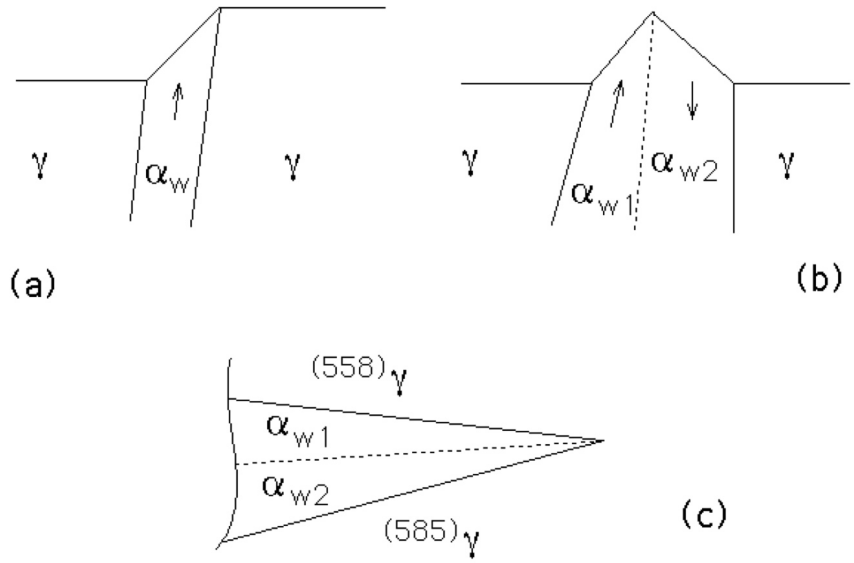

FIGURE 21. (a) A single invariant–plane strain shape deformation. (b) The combined effect of two mutually accommodating, back–to–back IPS deformations. (c) The morphology of two plates, with different habit plane variants, growing together in a mutually accommodating manner.

the austenite, together form the thin–wedge shaped plate which is characteristic of Widmanstätten ferrite.

Because Widmanstätten ferrite forms at low undercoolings (and above the T_0 temperature), it is thermodynamically required that the carbon is redistributed during growth. α_w therefore always has a paraequilibrium carbon content and grows at a rate which is controlled by the diffusion of carbon in the austenite ahead of the plate–tip. For plates, diffusion–controlled growth can occur at a constant rate because solute is partitioned to the sides of the plate, whereas the growing tip can advance into fresh austenite. Since the transformation is, nevertheless, displacive, substitutional atoms do not partition and an atomic correspondence is maintained between the parent and product lattices for all atoms other than carbon.

4.3. **Growth Kinetics.** For isothermal transformation during growth in which there is no partitioning of substitutional solutes, the growth rate is governed by the rate at which carbon diffuses ahead of the Widmanstätten ferrite plate tip. In the first approximation, the concentrations at the interface are given by a tie-lie of the phase

diagram as shown in Fig. 22. The diffusion flux of solute from the interface must equal the rate at which solute is incorporated in the precipitate so that:

$$\underbrace{(c^{\gamma\alpha} - c^{\alpha\gamma})\frac{\partial z^*}{\partial t}}_{\text{rate solute partitioned}} = \underbrace{-D\frac{\partial c}{\partial z}}_{\text{diffusion flux from interface}} \simeq D\frac{c^{\gamma\alpha} - \overline{c}}{\Delta z} \tag{4}$$

where z is a coordinate normal to the interface with a value z^* at the position of the interface. Note that concentration gradient here is assumed to be constant but it is in general evaluated at the position of the interface ($z = z^*$).

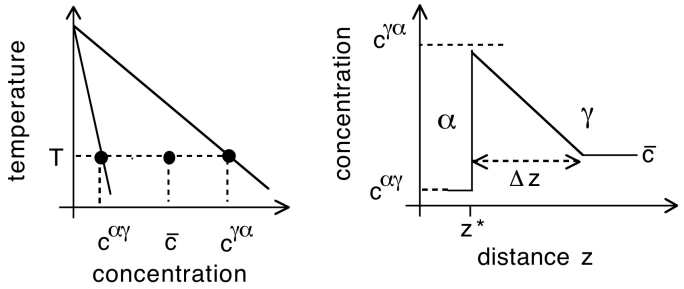

FIGURE 22. Phase diagram and its relationship to the concentration profile at the α/γ interface during diffusion-controlled growth.

The plate can be described as a parabolic cylinder in three dimensions (Fig. 23), a shape which is preserved as the plate lengthens. If it is assumed that the diffusion distance Δz is equal to the plate tip radius r (Fig. 23), then from equation 4 it follows that the lengthening rate $v_l = \partial z^*/\partial t$ is given by

$$v_l \approx \frac{D}{r}\frac{c^{\gamma\alpha} - \overline{c}}{c^{\gamma\alpha} - c^{\alpha\gamma}}. \tag{5}$$

This leads to the obvious difficulty that $v_l \to \infty$ as $r \to 0$, caused by the fact that the creation of additional interfacial area as the plate grows is neglected in the derivation. Given that the change in surface area per atom added to the plate is v_a/r, the corresponding increase in the free energy per atom due to the creation of additional interface is $\sigma v_a/r$ where σ is the interfacial energy per unit area and v_a is the volume per atom. Therefore, the net free energy change per atom, Δg_r, as the plate grows is

$$\Delta g_r = \Delta g_\infty - \frac{\sigma v_a}{r} \tag{6}$$

where Δg_∞ represents the free energy change per atom, driving the transformation in the absence of interface creation. At a critical radius r_c, $\Delta g_r = 0$ so that $\Delta g_\infty =$

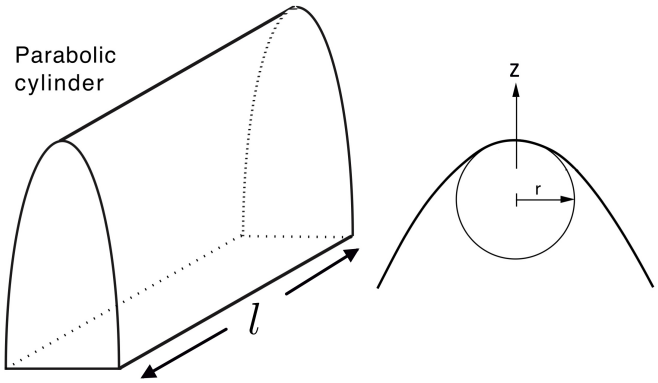

FIGURE 23. Widmanstätten ferrite plate represented as a parabolic cylinder, with tip radius r.

$\sigma v_a / r_c$ and $v_l = 0$. Equation 6 can therefore be written as

$$\Delta g_r = \frac{\sigma v_a}{r_c} - \frac{\sigma v_a}{r} \qquad \text{or} \qquad \frac{\Delta g_r}{\Delta g_\infty} = 1 - \frac{r_c}{r} \tag{7}$$

The velocity scales with the driving force when the latter is small, so equation 5 can be rewritten to account for the interface creation as follows:

$$v_l \approx \frac{D}{r}\left(\frac{c^{\gamma\alpha} - \overline{c}}{c^{\gamma\alpha} - c^{\alpha\gamma}}\right) \times \left(1 - \frac{r_c}{r}\right) \tag{8}$$

The accounting for interfacial energy in this manner is known as the *capillarity effect* [1] which governs the equilibrium between a curved particle and the matrix. Fig. 24 shows how the lengthening rate now goes through a maximum, and it is often assumed that the plate picks a radius consistent with the maximum growth rate. This is approximately consistent with experimental measurements as shown in Fig. 24b [2].

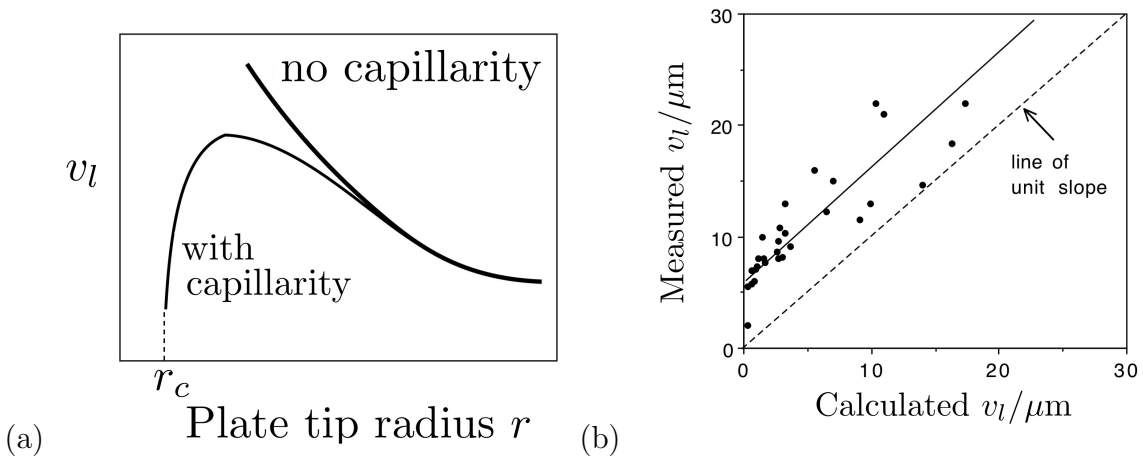

FIGURE 24. (a) Influence of interface curvature on plate lengthening rate. (b) Comparison of measured versus calculated lengthening rates.

4.4. **Summary.**

- An atomic correspondence is maintained for substitutional solutes, consistent with a displacive transformation mechanism.
- Ferrite has a paraequilibrium carbon content during growth which occurs at a constant rate, controlled by the diffusion of carbon in the austenite ahead of the plate tip.
- Growth involves the simultaneous and cooperative formation of a pair of adjacent, self–accommodating plates of Widmanstätten ferrite.

5. Allotriomorphic Ferrite

An allotriomorph has a shape which does not reflect its internal crystalline symmetry. This is because it tends to nucleate at the austenite grain surfaces, forming layers which follow the grain boundary contours (Fig. 25).

An idiomorph on the other hand, has a shape which reflects the symmetry of the crystal as embedded in the austenite. Idiomorphs nucleate without contact with the austenite grain surfaces; they tend to nucleate heterogeneously on non–metallic inclusions present in the steel.

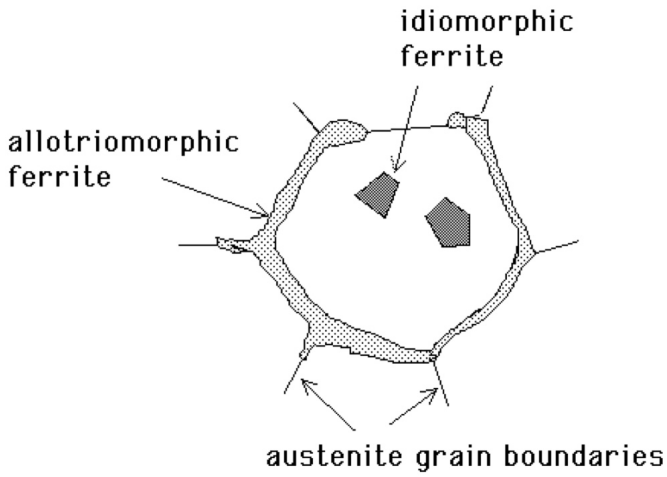

Figure 25. Allotriomorphic & idiomorphic ferrite.

These are both true diffusional transformations, *i.e.,* there is no atomic correspondence between the parent and product crystals, there is no invariant–plane strain shape change accompanying transformation, the growth rate is either diffusion–controlled, interface–controlled or mixed. Thermal activation is necessary for transformation, which can therefore only occur at high homologous temperatures.

The α/γ interface need not in this case be glissile; the motion of the interface involves diffusion and is not conservative.

5.1. **Revision of Diffusion–Controlled Growth in Fe–C.** The ferrite has a different chemical composition from the austenite in which it grows. We shall assume that the growth of ferrite (α) is controlled by the diffusion of carbon in the austenite (γ) ahead of the interface.

As the ferrite grows, so does the extent of its diffusion field. This retards growth because the solute then has to diffuse over ever larger distances. As we will prove, the thickness of the ferrite increases with the square root of time, *i.e.,* the growth rate slows down as time increases. We will assume in our derivation that the concentration gradient in the matrix is constant, and that the far–field concentration $\overline{c}$ never changes (*i.e.,* the matrix is semi–infinite normal to the advancing interface). This is to simplify the mathematics without loosing any of the insight into the problem.

For isothermal transformation in a binary alloy, the concentrations at the interface are given by a tie–lie of the phase diagram as shown in Fig. 26. The diffusion flux of solute from the interface must equal the rate at which solute is incorporated in the precipitate so that:

$$\underbrace{(c^{\gamma\alpha} - c^{\alpha\gamma})\frac{\partial z^*}{\partial t}}_{\text{rate solute partitioned}} = \underbrace{-D\frac{\partial c}{\partial z}}_{\text{diffusion flux from interface}} \simeq -D\frac{\overline{c} - c^{\gamma\alpha}}{\Delta z} \tag{9}$$

where z is a coordinate normal to the interface with a value z^* at the position of the interface. Note that the concentration gradient is evaluated at the position of the interface ($z = z^*$).

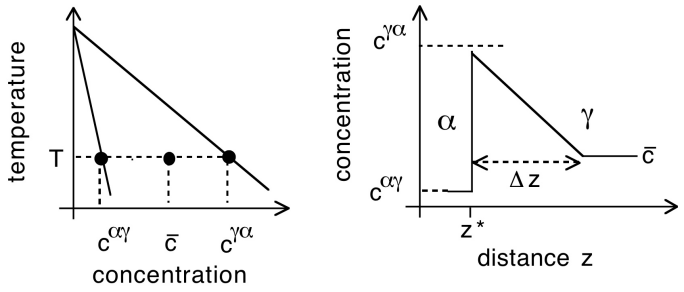

FIGURE 26. Phase diagram and its relationship to the concentration profile at the ferrite/austenite interface during diffusion–controlled growth.

A second equation can be derived by considering the overall conservation of mass:

$$(c^{\alpha\gamma} - \overline{c})z^* = \frac{1}{2}(\overline{c} - c^{\gamma\alpha})\Delta z \tag{10}$$

On combining these expressions to eliminate Δz we get:

$$\frac{\partial z^*}{\partial t} = \frac{D(\overline{c} - c^{\gamma\alpha})^2}{2z^*(c^{\alpha\gamma} - c^{\gamma\alpha})(c^{\alpha\gamma} - \overline{c})} \tag{11}$$

It follows that

$$z^* \propto \sqrt{Dt}$$

5.2. **Thermodynamics of Irreversible Processes.** Thermodynamics generally deals with measurable properties of materials, formulated on the basis of equilibrium. Thus, properties such as entropy and free energy are, on an appropriate scale, static and time–invariant during equilibrium. There are other parameters not relevant to the discussion of equilibrium: thermal conductivity, diffusivity and viscosity, but which are interesting because they can describe a second kind of time–independence, that of the steady–state. Thus, the concentration profile does not change during steady–state diffusion, even though energy is being dissipated by the diffusion.

The thermodynamics of irreversible processes deals with systems which are not at equilibrium but are nevertheless *stationary*. The theory in effect uses thermodynamics to deal with *kinetic* phenomena. There is nevertheless, a distinction between the thermodynamics of irreversible processes and kinetics. The former applies strictly to the steady–state, whereas there is no such restriction on kinetic theory.

5.2.1. *Reversibility.* A process whose direction can be changed by an infinitesimal alteration in the external conditions is called reversible. Consider the example illustrated in Fig. 27, which deals with the response of an ideal gas contained at uniform pressure within a cylinder, any change being achieved by the motion of the piston. For any starting point on the P/V curve, if the application of an infinitesimal force causes the piston to move slowly to an adjacent position still on the curve, then the process is reversible since energy has not been dissipated. The removal of the infinitesimal force will cause the system to revert to its original state.

On the other hand, if there is friction during the motion of the piston, then deviations occur from the P/V curve as illustrated by the cycle in Fig. 27. An infinitesimal force cannot move the piston because energy is dissipated due to friction (as given by the area within the cycle). Such a process, *which involves the dissipation of energy*, is classified as irreversible with respect to an infinitesimal change in the external conditions.

More generally, reversibility means that it is possible to pass from one state to another without appreciable deviation from equilibrium. Real processes are not reversible so equilibrium thermodynamics can only be used approximately, though the same thermodynamics defines whether or not a process can occur spontaneously without ambiguity.

For irreversible processes the *equations* of classical thermodynamics become *inequalities*. For example, at the equilibrium melting temperature, the free energies of the

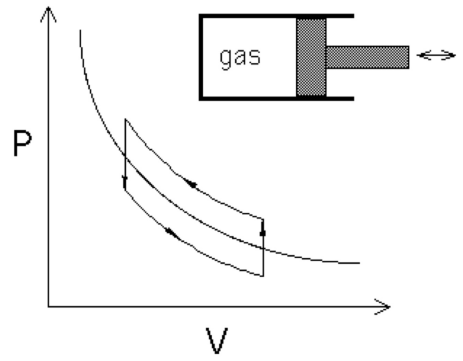

FIGURE 27. The curve represents the variation in pressure within the cylinder as the volume of the ideal gas is altered by positioning the frictionless piston. The cycle represents the dissipation of energy when the motion of the piston causes friction.

pure liquid and solid are identical ($G_{liquid} = G_{solid}$) but not so below that temperature ($G_{liquid} > G_{solid}$). Such inequalities are much more difficult to deal with though they indicate the natural direction of change. For steady–state processes however, the thermodynamic framework for irreversible processes as developed by Onsager is particularly useful in approximating relationships even though the system is not at equilibrium.

5.2.2. *The Linear Laws.* At equilibrium there is no change in entropy or free energy. An irreversible process dissipates energy and entropy is created continuously. In the example illustrated in Fig. 27, the dissipation was due to friction; diffusion ahead of a moving interface is dissipative. The rate at which energy is dissipated is the product of the temperature and the rate of entropy production (*i.e.* $T\sigma$) with:

$$T\sigma = JX \tag{12}$$

where J is a generalised flux of some kind, and X a generalised force. In the case of an electrical current, the heat dissipation is the product of the current (J) and the electromotive force (X).

As long as the flux–force sets can be expressed as in equation 12, the flux must naturally depend in some way on the force. It may then be written as a function $J\{X\}$ of the force X. At equilibrium, the force is zero. If $J\{X\}$ is expanded in a Taylor series about equilibrium ($X = 0$), we get

$$\begin{aligned} J\{X\} &= \sum_{0}^{\infty} a_n X^n \\ &= J\{0\} + J'\{0\}\frac{X}{1!} + J''\{0\}\frac{X^2}{2!}\ldots \end{aligned} \tag{13}$$

Note that $J\{0\} = 0$ since that represents equilibrium. If the high order terms are neglected then we see that

$$J \propto X.$$

This is a key result from the theory, that the forces and their conjugate fluxes are linearly related ($J \propto X$) whenever the dissipation can be written as in equation 13, at least when the deviations from equilibrium are not large.

Consider for example, a closed system in which a quantity $\mathrm{d}H$ of heat is transferred in a time interval $\mathrm{d}t$ across an area A in a direction z normal to that area, from a region at temperature T_h to a lower temperature T_ℓ. The receiving part increases its entropy by $\mathrm{d}H/T_\ell$ whereas the depleted region experiences a reduction $\mathrm{d}H/T_\mathrm{H}$, so that the change in entropy is

$$\mathrm{d}S = \mathrm{d}H\left(\frac{1}{T_\ell} - \frac{1}{T_\mathrm{h}}\right).$$

The rate of entropy production per unit volume is therefore

$$\sigma = \frac{1}{V}\frac{\mathrm{d}S}{\mathrm{d}t} = \frac{1}{V}\frac{\mathrm{d}H}{\mathrm{d}t}\left(\frac{1}{T_\ell} - \frac{1}{T_\mathrm{h}}\right). \tag{14}$$

The flux of heat J is defined as $A^{-1}\mathrm{d}H/\mathrm{d}t$ so Equation 14 becomes

$$\sigma = J\frac{A}{V}\left(\frac{1}{T_\ell} - \frac{1}{T_\mathrm{h}}\right) \equiv J\left(-\frac{1}{T^2}\right)\frac{\mathrm{d}T}{\mathrm{d}z} \qquad \text{or} \qquad T\sigma = \underbrace{J}_{\text{flux}}\underbrace{\left(-\frac{1}{T}\right)\frac{\mathrm{d}T}{\mathrm{d}z}}_{\text{force}}$$

Examples of forces and fluxes in the context of the present theory are listed in Table 4.

TABLE 4. Examples of forces and their conjugate fluxes. z is distance, ϕ is the electrical potential, and μ is a chemical potential.

Force	Flux
$-\frac{\partial\phi}{\partial z}$	Electrical Current
$-\frac{1}{T}\frac{\partial T}{\partial z}$	Heat flux
$-\frac{\partial\mu_i}{\partial z}$	Diffusion flux
Stress	Strain rate

5.2.3. *Multiple Irreversible Processes.* There are many circumstances in which a number of irreversible processes occur together. In a ternary Fe–Mn–C alloy, the diffusion flux of carbon depends not only on the gradient of carbon, but also on that of manganese. Thus, a uniform distribution of carbon will tend to become inhomogeneous in the presence of a manganese concentration gradient. Similarly, the flux of heat may not depend on the temperature gradient alone; heat can be driven also by an electromotive force (Peltier effect)[2]. Electromigration involves diffusion driven by an electromotive force. When there is more then one dissipative process, the total energy dissipation rate can still be written

$$T\sigma = \sum_i J_i X_i. \tag{15}$$

In general, if there is more than one irreversible process occurring, it is found *experimentally* that each flow J_i is related not only to its conjugate force X_i, but also is related linearly to all other forces present. Thus,

$$J_i = M_{ij} X_j \tag{16}$$

with $i,\ j = 1, 2, 3 \ldots$. Therefore, a given flux depends on all the forces causing the dissipation of energy.

5.2.4. *Onsager Reciprocal Relations.* Equilibrium in real systems is always dynamic on a microscopic scale. It seems obvious that to maintain equilibrium under these dynamic conditions, a process and its reverse must occur at the same rate on the microscopic scale. The consequence is that provided the forces and fluxes are chosen from the dissipation equation and are independent, $M_{ij} = M_{ji}$. This is known as the Onsager theorem, or the Onsager reciprocal relations. It applies to systems near equilibrium when the properties of interest have even parity, and assuming that the fluxes and their corresponding forces are independent. An exception occurs with magnetic fields in which case there is a sign difference $M_{ij} = -M_{ji}$.

5.3. **Ternary Steels.** Consider now a ternary steel, say Fe–Mn–C. It would be necessary to satisfy two equations of the form of equation 1, simultaneously, for each of the solutes:

$$\begin{aligned} (c_1^{\gamma\alpha} - c_1^{\alpha\gamma})v &= -D_1 \nabla c_1 \\ (c_2^{\gamma\alpha} - c_2^{\alpha\gamma})v &= -D_2 \nabla c_2 \end{aligned} \tag{17}$$

where the subscripts refer to the solutes (1 for carbon and 2 for Mn). The interface velocity v is the $\partial z^*/\partial t$ in equation 11.

[2]In the Peltier effect, the two junctions of a thermocouple are kept at the same temperature but the passage of an electrical current causes one of the junctions to absorb heat and the other to liberate the same quantity of heat. This Peltier heat is found to be proportional to the current.

Because $D_1 \gg D_2$, these equations cannot in general be simultaneously satisfied for the tie–line passing through the alloy composition $\overline{c}_1, \overline{c}_2$. It is, however, possible to choose other tie–lines which satisfy equation 17. If the tie–line is such that $c_1^{\gamma\alpha} = \overline{c}_1$ (*e.g.* line *cd* for alloy A of Fig. 28a), then ∇c_1 will become very small, the driving force for carbon diffusion in effect being reduced, so that the flux of carbon atoms is forced to slow down to a rate consistent with the diffusion of manganese. Ferrite forming by this mechanism is said to grow by a 'Partitioning, Local Equilibrium' (or PLE) mechanism, in recognition of the fact that $c_2^{\alpha\gamma}$ can differ significantly from $\overline{c}_2$, giving considerable partitioning and long–range diffusion of manganese into the austenite.

An alternative choice of tie–line could allow $c_2^{\alpha\gamma} \rightarrow \overline{c}_2$ (*e.g.* line *cd* for the alloy of Fig. 28b), so that ∇c_2 is drastically increased since only very small amounts of Mn are partitioned into the austenite. The flux of manganese atoms at the interface correspondingly increases and manganese diffusion can then keep pace with that of carbon, satisfying the mass conservation conditions of equation 17. The growth of ferrite in this manner is said to occur by a 'Negligible Partitioning, Local Equilibrium' (or NPLE) mechanism, in recognition of the fact that the manganese content of the ferrite approximately equals $\overline{c}_2$, so that little if any manganese partitions into austenite.

What circumstances determine whether growth follows the PLE or NPLE mode? Fig. 29 shows the Fe–Mn–C phase diagram, now divided into domains where either PLE or NPLE is possible but not both. The domains are obtained by drawing right–handed triangles on each tie–line in the $\alpha + \gamma$ phase field and joining up all the vertices. For example, prove to yourself that if you attempt to define NPLE conditions in the PLE domain, then the tie–line determining interface compositions will incorrectly show that both austenite and ferrite contain less carbon than $\overline{c}_1$, a circumstance which is physically impossible.

Paraequilibrium is a constrained equilibrium. It occurs at temperatures where the diffusion of substitutional solutes is not possible within the time scale of the experiment. Nevertheless, interstitials may remain highly mobile. Thus, in a steel, manganese does not partition between the ferrite and austenite, but subject to that constraint, the carbon redistributes until it has the same chemical potential in both phases.

Therefore, the tie–lines in the phase diagram (Fig. 30) are all virtually parallel to the carbon axis, since Mn does not partition between ferrite and austenite.

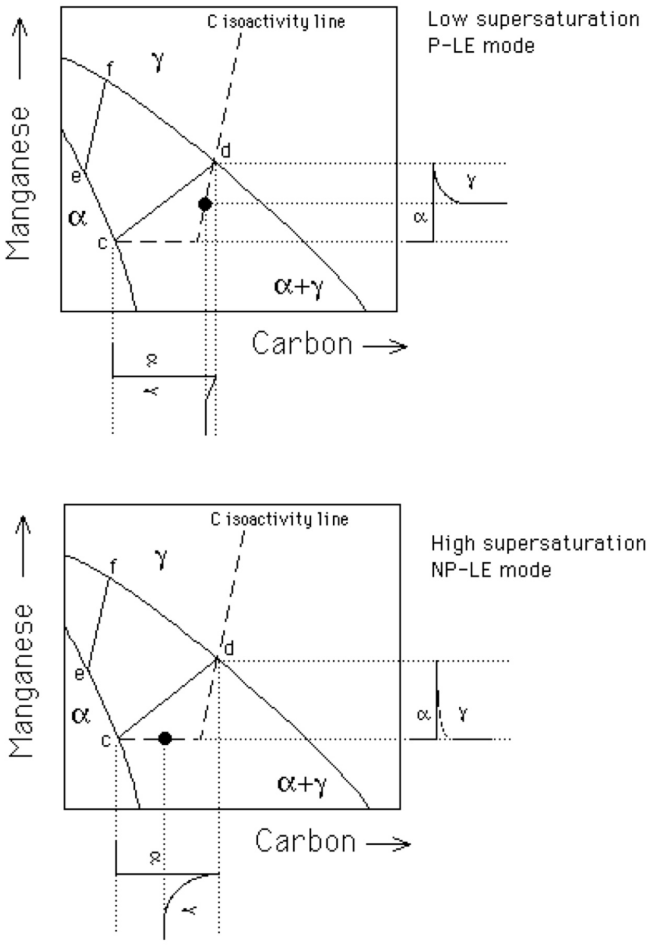

FIGURE 28. Schematic isothermal sections of the Fe–Mn–C system, illustrating ferrite growth occurring with local equilibrium at the α/γ interface. (a) Growth at low supersaturations (P–LE) with bulk redistribution of manganese, (b) growth at high supersaturations (NP–LE) with negligible partitioning of manganese during transformation. The bulk alloy compositions are designated by the symbol • in each case.

Prove to yourself that in an isothermal section of the ternary phase diagram, the paraequilibrium phase boundaries must lie within the equilibrium phase boundaries as illustrated in Fig. 31.

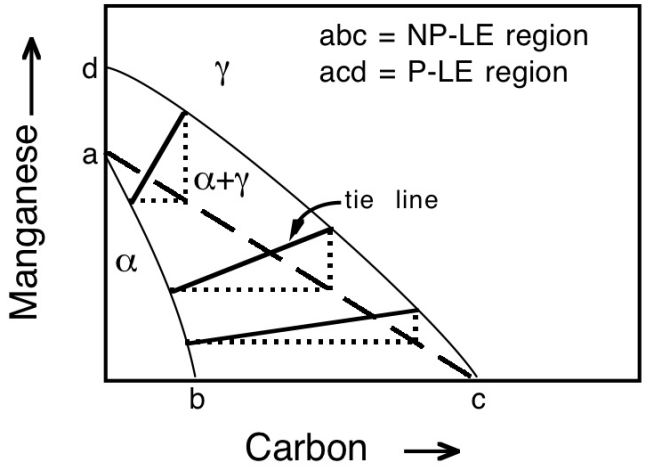

FIGURE 29. Regions of the two–phase field where either PLE or NPLE modes of transformation are possible.

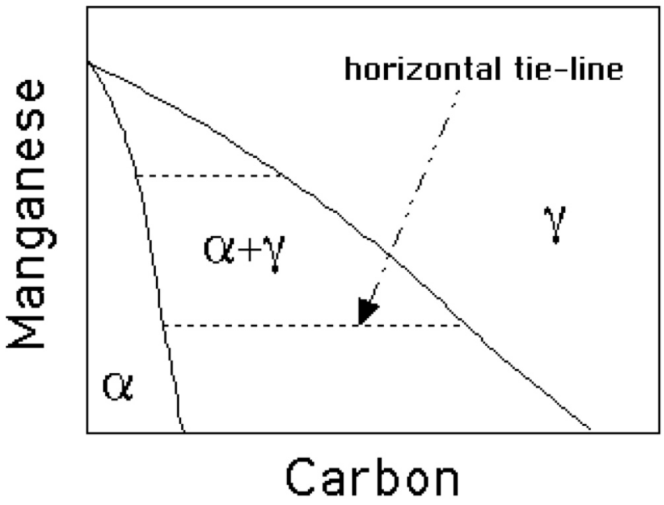

FIGURE 30. A paraequilibrium phase diagram.

6. PEARLITE

A colony of pearlite when viewed in three dimensions consists of an interpenetrating bicrystal of ferrite and cementite. In planar sections the phases appear as lamellae which grow at a common front with the austenite. Cementite (θ) is rich in carbon whereas ferrite (α) accommodates very little when it is in equilibrium with either

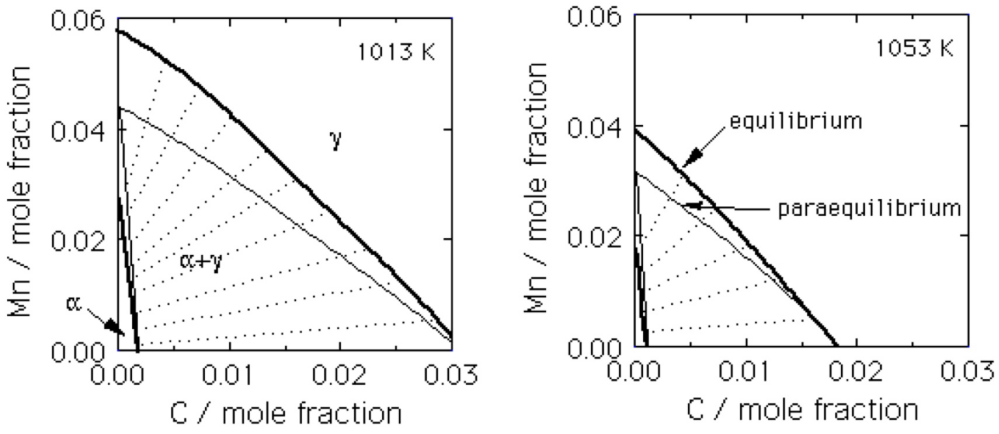

FIGURE 31. The paraequilibrium phase field lies within the equilibrium field. The tie–lines illustrated are for equilibrium.

cementite or austenite (γ). It is therefore necessary for carbon to be redistributed at the transformation front. This can happen either by diffusion in the austenite in a direction parallel to the transformation front (Fig. 32).

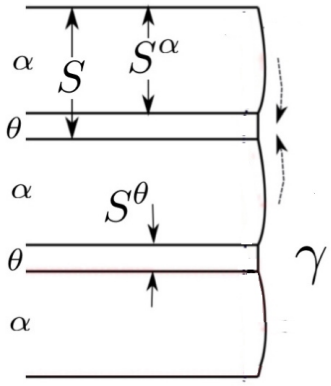

FIGURE 32. Diffusion flux parallel to the advancing interface. S is the interlamellar spacing.

The diffusion distance parallel to the interface can be approximated as aS where a is a constant and S is the interlamellar spacing. By analogy with equation 9, it follows that the rate at which solute is absorbed by the cementite must equal the amount arriving there by diffusion, so that

$$v(c^{\theta} - c^{\gamma\theta}) = D\frac{c^{\gamma\alpha} - c^{\gamma\theta}}{aS} \tag{18}$$

where v is the speed of the growth front, D is the diffusivity of carbon in austenite and the concentration terms are self–explanatory.

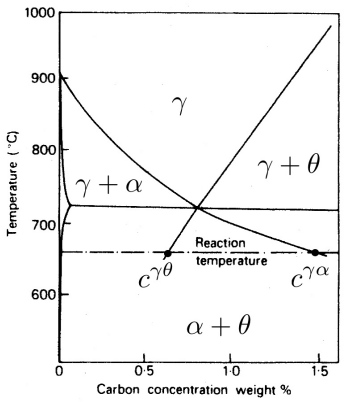

FIGURE 33. Phase diagram with extrapolated phase boundaries to identify the concentrations in the austenite which is in equilibrium with cementite or ferrite.

However, there is an additional process which consumes energy, the creation of cementite/ferrite interfaces within the pearlite colony. The minimum value of interlamellar spacing possible is a critical spacing $S_C = 2\sigma^{\alpha\theta}/\Delta G$ where $\sigma^{\alpha\theta}$ is the interfacial energy per unit area and ΔG is the magnitude of the driving force for transformation in Joules per unit volume. Growth ceases when $S = S_C$. To allow for the energy consumed in the process of interface creation, equation 18 is modified by a term $1 - [S_C/S]$ as follows:

$$v = \frac{D}{aSS_C}\frac{c^{\gamma\alpha} - c^{\gamma\theta}}{(c^{\theta} - c^{\gamma\theta})}\left(1 - \frac{S_C}{S}\right) \tag{19}$$

We now need to specify the value that S will adopt during growth, and one assumption is that the spacing will correspond to that consistent with the maximum growth rate, *i.e.* when $S = 2S_C$.

The theory presented here is necessarily oversimplified and uses a number of unnecessary assumptions; more rigorous models are available but get extremely complex as soon as interfacial diffusion and the influence of solutes other than carbon is taken into consideration.

7. Overall Transformation Kinetics

7.1. **Isothermal Transformation.** To model transformation it is obviously necessary to calculate the nucleation and growth rates, but an estimation of the volume fraction requires *impingement* between particles to be taken into account.

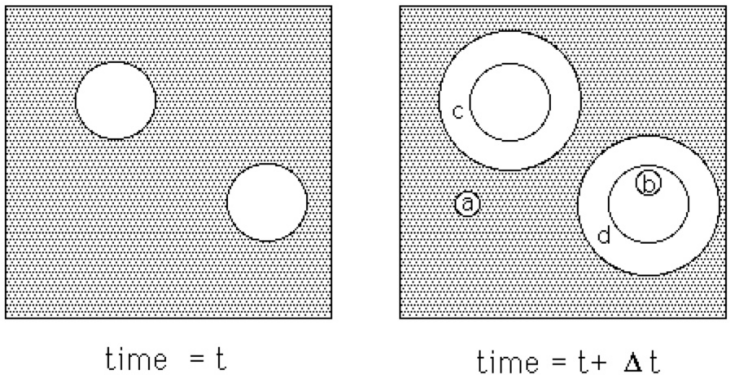

Figure 34. An illustration of the concept of extended volume. Two precipitate particles have nucleated together and grown to a finite size in the time t. New regions c and d are formed as the original particles grow, but a & b are new particles, of which b has formed in a region which is already transformed.

This is done using the extended volume concept of Kolmogorov, Johnson, Mehl and Avrami. Referring to Fig. 34, suppose that two particles exist at time t; a small interval δt later, new regions marked a, b, c & d are formed assuming that they are able to grow unrestricted in extended space whether or not the region into which they grow is already transformed. However, only those components of a, b, c & d which lie in previously untransformed matrix can contribute to a change in the real volume of the product phase (α) :

$$dV^{\alpha} = \left(1 - \frac{V^{\alpha}}{V}\right) dV_e^{\alpha} \tag{20}$$

where it is assumed that the microstructure develops at random. The subscript e refers to extended volume, V^{α} is the volume of α and V is the total volume. Multiplying the change in extended volume by the probability of finding untransformed regions has the effect of excluding regions such as b, which clearly cannot contribute to the real change in volume of the product. For a random distribution of precipitated particles, this equation can easily be integrated to obtain the real volume

fraction,

$$\frac{V^\alpha}{V} = 1 - \exp\left\{-\frac{V_e^\alpha}{V}\right\} \tag{21}$$

The extended volume V_e^α is straightforward to calculate using nucleation and growth models and neglecting completely any impingement effects. Consider a simple case where the α grows isotropically at a constant rate G and where the nucleation rate per unit volume, I_V. The volume of a particle nucleated at time $t = \tau$ (Fig. 35) is given by

$$v_\tau = \frac{4}{3}\pi G^3(t-\tau)^3 \tag{22}$$

The change in extended volume over the interval τ and $\tau + d\tau$ is

$$dV_e^\alpha = \frac{4}{3}\pi G^3(t-\tau)^3 \times I_V \times V \times d\tau \tag{23}$$

On substituting into equation 21 and writing $\xi = V^\alpha/V$, we get

$$dV^\alpha = \left(1 - \tfrac{V^\alpha}{V}\right)\tfrac{4}{3}\pi G^3(t-\tau)^3 I_V V \; d\tau$$

$$\text{so that} \qquad -\ln\{1-\xi\} = \tfrac{4}{3}\pi G^3 I_V \int_0^t (t-\tau)^3 \; d\tau$$

$$\text{and} \qquad \xi = 1 - \exp\{-\pi G^3 I_V t^4/3\} \tag{24}$$

This equation has been derived for the specific assumptions of random nucleation, a constant nucleation rate and a constant growth rate. There are different possibilities but they often reduce to the general form:

$$\xi = 1 - \exp\{-k_A t^n\} \tag{25}$$

where k_A and n characterise the reaction as a function of time, temperature and other variables. The values of k_A and n can be obtained from experimental data by plotting $\ln(-\ln\{1-\xi\})$ versus $\ln\{t\}$. The specific values of k_A and n depend on the nature of nucleation and growth. Clearly, a constant nucleation and growth rate leads to a time exponent $n = 4$, but if it is assumed that the particles all begin growth instantaneously from a fixed number density of sites (i.e., nucleation is not needed) the $n = 3$ when the growth rate is constant. There are other scenarios and the values of the Avrami parameters are not necessarily unambiguous in the sense that the same exponent can represent two different mechanisms.

The form of equation 25 is illustrated in Fig. 36. Note that the effect of temperature is to alter the thermodynamic driving force for transformation, to alter diffusion

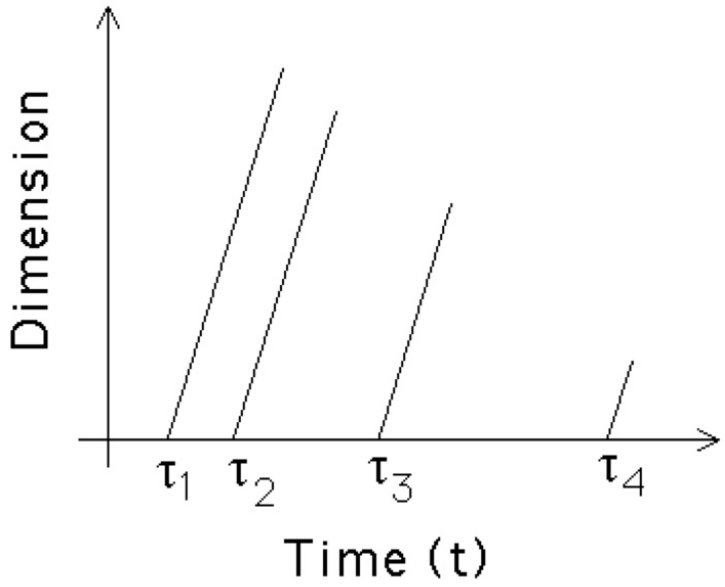

FIGURE 35. An illustration of the incubation time τ for each particle.

coefficients and to influence any other thermally activated processes. The effect of manganese is via its influence on the stability of the parent and product phases.

The results of many isothermal transformation curves such as the ones illustrated in Fig. 36 can be plotted on at time–temperature–transformation diagram as illustrated in Fig. 37. The curves typically have a C shape because the driving force for transformation is small at high temperatures whereas the diffusion coefficient is small at low temperatures. There is an optimum combination of these two parameters at intermediate temperatures, giving a maximum in the rate of reaction. The curve marked *start* corresponds to a detectable limit of transformation (e.g., 5%), and that marked finish corresponds to say 95% transformation.

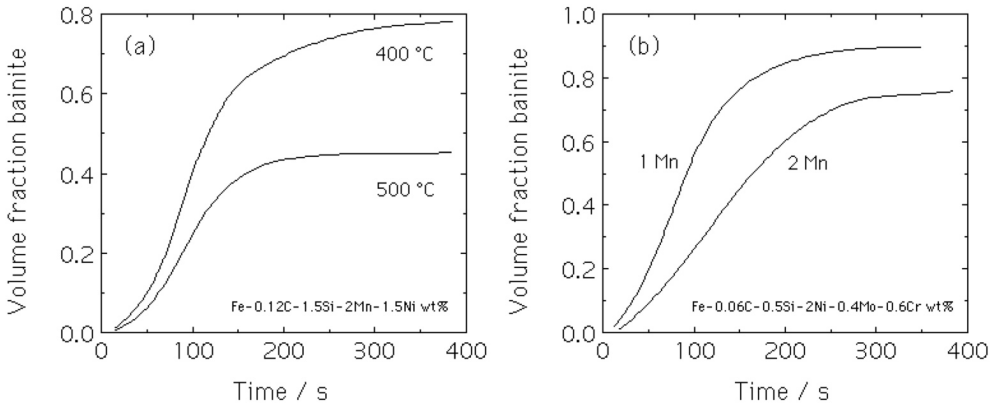

FIGURE 36. The calculated influence of (a) transformation temperature and (b) manganese concentration on the kinetics of the bainite reaction (Singh, 1998). Bainite is a particular kind of solid–state phase transformation that occurs in steels.

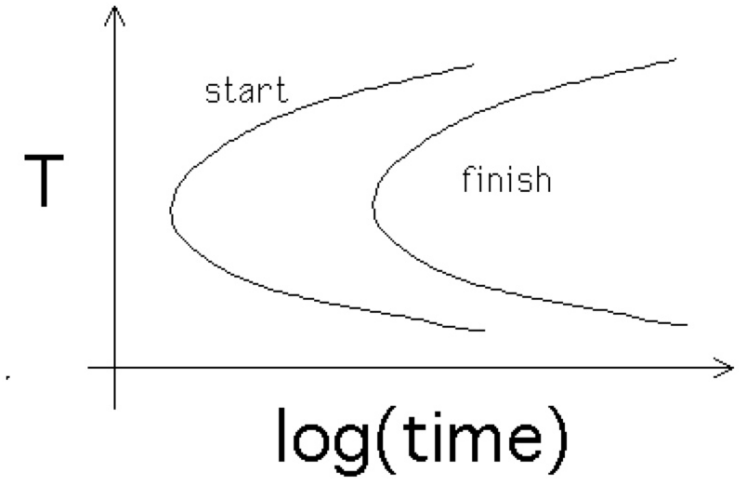

FIGURE 37. A time–temperature–transformation (TTT) diagram.

8. TRIP Steels

The steels developed to exploit the properties obtained when the martensite reaction occurs during plastic deformation are known as *transformation-induced plasticity* (TRIP) steels [3]. The way in which they enhance the strength and uniform ductility of the steel is discussed later, but suffice it to say that a significant constituent of the microstructure must be austenite which is capable of transforming into martensite under the influence of an applied stress. Some of the original studies were conducted on alloys rich in solutes in order to preserve the austenite to ambient temperature; this can be expensive, but is a good starting point for the discussion of the TRIP effect.

As pointed out in section 1, martensitic transformation is also a deformation, described accurately as an invariant-plane strain with a shear s on the habit plane, and a dilatation δ normal to that plane, Fig. 38. Given the orthonormal coordinate system Z defined by the the unit vectors $\mathbf{z}_1$ parallel to the direction of shear, and $\mathbf{z}_3$ normal to the habit plane, the deformation matrix $\mathbf{P}$ becomes:

$$\left(\mathrm{Z} \quad \mathbf{P} \quad \mathrm{Z}\right) = \begin{pmatrix} 1 & 0 & s \\ 0 & 1 & 0 \\ 0 & 0 & 1+\delta \end{pmatrix}. \tag{26}$$

The effect of the deformation on any vector $\mathbf{u}$ to produce a resultant vector $\mathbf{v}$ is then given by

$$\left(\mathrm{Z} \quad \mathbf{P} \quad \mathrm{Z}\right) [\mathrm{Z}; \mathbf{u}] = [\mathrm{Z}; \mathbf{v}] \tag{27}$$

The two vectors will not in general be parallel, but a comparison of the magnitudes gives an impression of the strain expected due to martensitic transformation. This

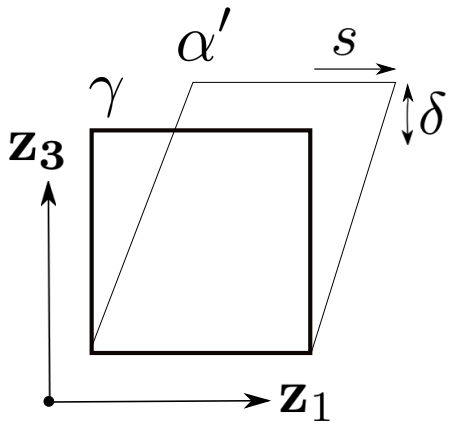

FIGURE 38. Coordinate axes for the derivation of the deformation matrix representing martensitic transformation (α') from austenite (γ).

calculation of strain is along a specific direction $\mathbf{u}$, due to the shape deformation

associated with the formation of a plate of martensite. In dealing with TRIP steels, the problem needs to be posed somewhat differently, i.e., what is the strain along a particular direction when a stress is applied to induce martensitic transformation in an otherwise stable austenite. It is necessary therefore to consider the thermodynamics of stress-affected martensitic transformation. Fig. 39 shows that in the absence of external stress ($\sigma = 0$), the martensite-start temperature M_S is defined by the temperature at which the free energy change $\Delta G^{\gamma\alpha}$ when austenite decomposes into ferrite of the same composition, reaches a critical value ΔG_{M_S}.

In contrast, when transformation occurs under the influence of a stress, the latter interacts with the shape deformation and the interaction energy U is given by [4] to be:

$$U = \tau_\circ s + \sigma_N \delta \tag{28}$$

where $\tau_\circ$ is the shear stress on the habit plane and σ_N the stress normal to that plane. Notice that the strains involved are plastic, so the interaction energy is given simply by the product of the stress and strain, rather than half that value as is sometimes assumed on the basis of elastic strains. If the stress is such that it favours the formation of martensite then U supplements $\Delta G^{\gamma\alpha}$ and the martensite-start temperature is raised to M_S^σ which is above ambient temperature, so that stress-induced martensitic transformation becomes feasible (Fig. 39).

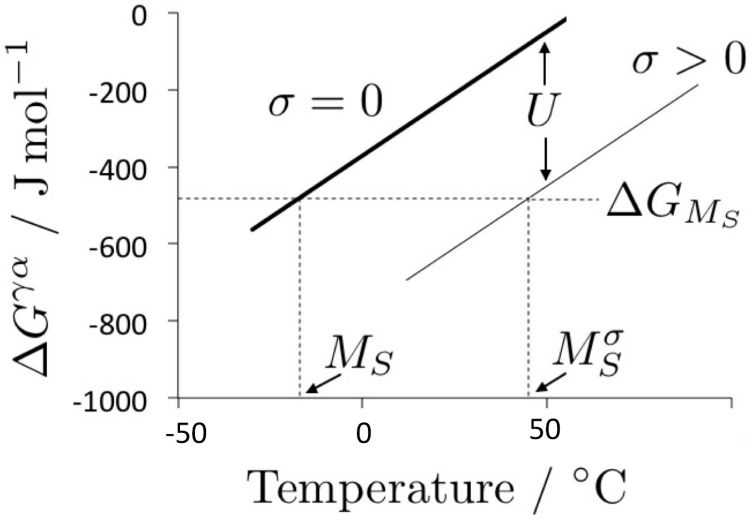

FIGURE 39. Plot of the chemical driving force for martensitic transformation against temperature, with σ representing the applied stress.

Each single crystal of austenite can in principle transform into 24 different crystallographic variants of martensite. Each of these variants is associated with a particular value of U depending on its orientation relative to the applied stress. Therefore, those variants with the largest interaction with the stress, i.e., which transform in a manner that relieves the stress, are favoured. This process is known as *variant selection* so that stress-induced martensite results in a biased microstructure with reduced variety. This is illustrated in Fig. 40, where the martensite is generated by applying a tensile stress to polycrystalline metastable austenite, resulting in plates which are approximately at 45° to the tensile axis.

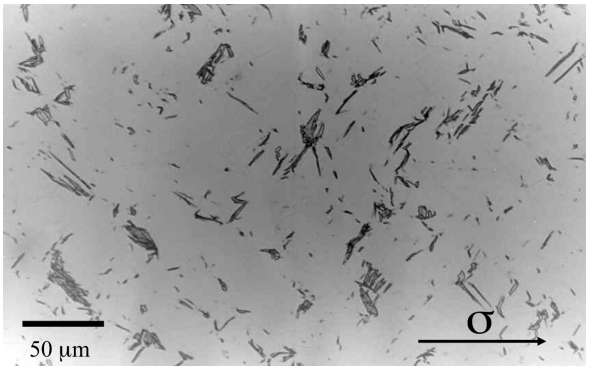

FIGURE 40. A non-random distribution of martensite habit-plane orientations produced by stress-induced martensitic transformation at a temperature between M_S and M_S^σ. The sample is polycrystalline austenite.

Assuming that a tensile stress σ_1 is applied, inclined at an angle θ to the habit plane normal, with the stress axis in the plane containing $\mathbf{z_1}$ and $\mathbf{z_3}$, then from equation 28 and the Mohr's circle representation in Fig 41,

$$U = \underbrace{\frac{\sigma_1}{2}\sin 2\theta}_{\tau_\circ} \times s + \underbrace{\frac{\sigma_1}{2}(1+\cos 2\theta)}_{\sigma_N} \times \delta$$

$$\frac{dU}{d\theta} = \frac{\sigma_1}{2}[2s\cos 2\theta - 2\delta \sin 2\theta] \tag{29}$$

Setting the differential to zero gives the maximum value of U at $\tan 2\theta_{\max} = s/\delta$, which for typical values of $s = 0.26$ and $\delta = 0.03$ gives $\theta_{\max} = 41.7°$. Given that there are 24 habit plane orientations within a single austenite grain, it is likely that one close to this value will form first, hence explaining the observation of aligned plates in Fig. 41 even though the sample has many orientations of austenite grains. The tensile axis can be represented as a unit vector

$$[\mathrm{Z}; \mathbf{u}] = [\sin\theta_{\max} \ 0 \ \cos\theta_{\max}]$$

and using $\theta = \theta_{\max}$, the elongation obtained along the tensile axis when a single crystal of austenite transforms completely into the most favoured orientation of

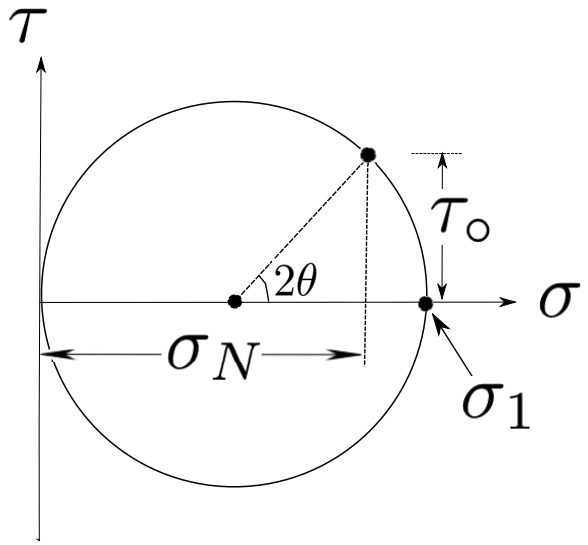

FIGURE 41. Mohr's circle representation of the shear and normal stresses on a habit plane normal inclined at θ to the tensile stress σ_1.

martensite is, using equation 27, given by:

$$\begin{aligned} [\mathrm{Z};\mathbf{v}] &= [(\sin\theta_{\max} + s\cos\theta_{\max})\ 0\ (1+\delta)\cos\theta_{\max}] \\ \text{elongation}\,\% &= \left(\frac{|\mathbf{v}|}{|\mathbf{u}|} - 1\right) \times 100 \end{aligned}$$

This assumes that $\mathbf{v}$ is parallel to $\mathbf{u}$ and a correction would be needed if there is a relative rotation. The elongation due to phase transformation is therefore calculated is found to be 15% [5]. This impressive value of elongation due to phase transformation alone supplements that due to ordinary dislocation plasticity, which can be a significant boon to the design of strong steels which usually suffer from early plastic instabilities. However, steels which are fully austenitic at ambient temperature can, in the context of iron-based alloys, be expensive.

8.1. **TRIP-Assisted Steels.** One way of producing cheap austenite is to stabilise it with carbon, but excessive carbon can harm other important engineering properties such as the ability to use the steel in a welded state. But an ingenious method involves a low-carbon steel ($\approx 0.15\,\mathrm{wt}\%$ C), which is first transformed into about 70% of allotriomorphic ferrite and the remaining austenite cooled to partly transform it into bainitic ferrite. Both of these transformations leave the residual austenite enriched in carbon to a concentration in excess of $1.2\,\mathrm{wt}\%$, thus leaving about 15% of retained austenite in the final microstructure. Since bainite is the last phase to form, the carbon concentration of the austenite is limited by the T_0 condition described in section 2.

It is because the steel is not fully austenitic, that it is referred to as *TRIP-assisted* and typically has a lean composition Fe–0.15C–1.5Si–1.5Mn wt%. The silicon serves to prevent the precipitation of cementite from the carbon-enriched austenite, and the manganese enhances the hardenability required to implement heat treatments suitable for mass production. The microstructure and typical properties are illustrated in Fig. 42, which also shows how the retained austenite transforms during the course of deformation.

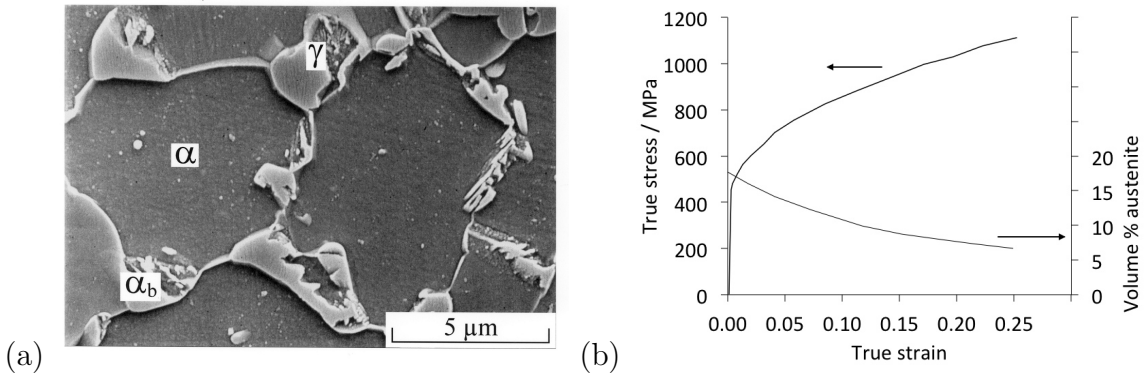

FIGURE 42. TRIP-assisted steel. (a) Typical final microstructure (micrograph courtesy of P. Jacques). (b) True stress versus true strain, and the stress-assisted decomposition of retained austenite [data from [6]].

The fraction of retained austenite in a TRIP-assisted steel is $V_\gamma = 0.20$ (Fig. 42, in which case the maximum elongation to be expected if it all transforms into the favoured crystallographic variant of martensite is, using equation 30 scaled with V_γ given by $0.15 \times 0.2 = 0.03$. The transformation strain therefore makes a negligible contribution to the overall elongation which is about 25% as shown in Fig. 42b. The major contribution from stress-affected transformation is not via the shape deformation of the martensite, but through a composite effect [5]. The production of hard, untempered martensite increases the work hardening rate and hence delays the onset of plastic instabilities. This is why TRIP-assisted steels have a large uniform elongation.

8.2. δ–**TRIP Steel.** In this alloying concept, δ–ferrite which forms during solidification is stabilised by specific aluminium additions, and substitutes for the 70% of allotriomorphic ferrite in conventional TRIP-assisted steels [7]. The advantage in doing this is that the δ-ferrite can never be fully removed from the microstructure so that a a fully martensitic structure cannot be produced in the heat–affected zone of

a resistance spot weld. Another benefit is that the aluminium substitutes for the role of silicon in suppressing cementite precipitation. The difficulty with silicon is that during hot processing, it forms a low-melting temperature oxide known as fayalite which adheres to the steel, making it difficult to remove other disfiguring oxides from the surface of the steel during de-scaling operations. Silicon can therefore lead to a reduction in the quality of the steel surface, and cause problems during coating processes. The chemical composition of the steel is typically Fe-0.4C-0.2Si-1Mn-3Al wt% and the microstructures obtained directly from casting and following processing are illustrated in Fig. 43.

(a)

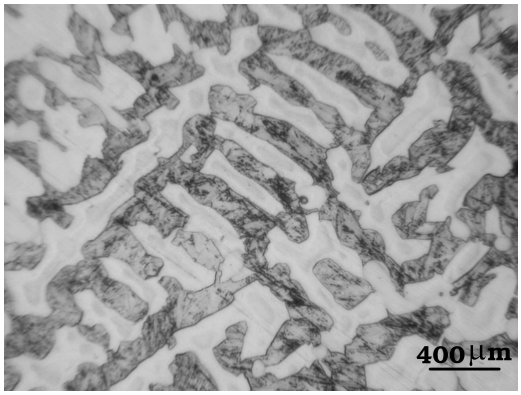

(b)

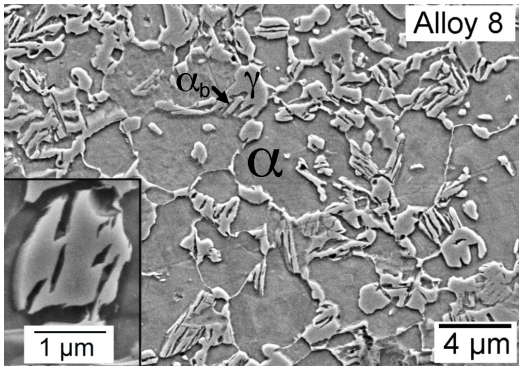

(c)

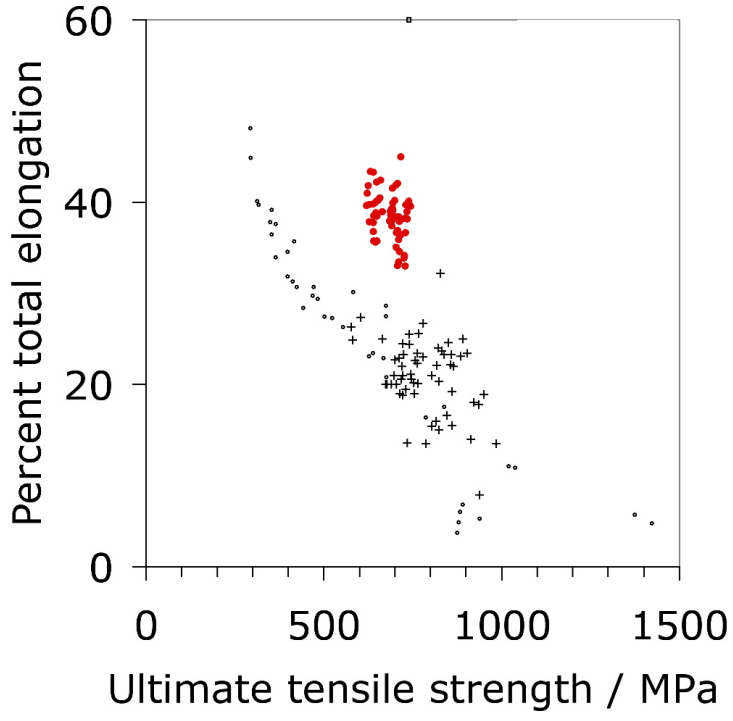

FIGURE 43. δ-TRIP steel. (a) Optical microstructure of the as-cast condition showing the δ-ferrite dendrites and martensite between the dendrite arms [7]. (b) The structure after processing to produce bainite and retained austenite [8]. (c) The properties obtained (in red) compared against a range of established automotive steels.

9. TWIP Steels

There are three essential modes by which steels can be permanently deformed at ambient temperature, without recourse to diffusion. Individual dislocations whose Burgers vectors correspond to lattice vectors can glide, leading to a change in shape without altering the crystal structure or volume. In contrast, a displacive transformation (*e.g.* martensite or bainite) results not only in a plastic strain, but also a change of crystal structure and density; this is the phenomenon exploited in the TRIP steels.

The third mode of deformation is mechanical twinning, in which the crystal structure of the steel is preserved but the twinned region is reoriented in the process. Mechanical twinning results in a much larger shear strain $s = 1/\sqrt{2}$, compared with displacive transformations where s is typically 0.25. There is a particular class of extraordinarily ductile alloys of iron, known as the TWIP steels, which exploit mechanical twinning to achieve their properties. "TWIP" stands for twinning-induced plasticity.

TWIP stands for twinning-induced plasticity. The alloys are austenitic and remain so during mechanical deformation, but the material is able to accommodate strain via both the glide of individual dislocations and through mechanical twinning on the $\{1\ 1\ 1\}_\gamma \langle 1\ 1\ \overline{2} \rangle_\gamma$ system. The alloys typically contain a large amount of manganese, some aluminium and silicon (*e.g.* Fe-25Mn-3Si-3Al wt%) with carbon and nitrogen present essentially as impurities. Larger concentrations of carbon may be added to enhance strength. At high manganese concentrations, there is a tendency for the austenite to transform into ϵ-martensite (hexagonal close packed) during deformation. ϵ-martensite can form by the dissociation of a perfect $a/2 \langle 0\ 1\ 1 \rangle_\gamma$ dislocation into Shockley partials on a close packed $\{1\ 1\ \overline{1}\}_\gamma$ plane, with a fault between the partials. This faulted region represents a three layer thick plate of ϵ-martensite. A reduction in the fault energy therefore favours the formation of this kind of martensite. The addition of aluminium counters this because it raises the stacking fault energy of the austenite. Silicon has the opposite effect of reducing the stacking fault energy, but like aluminium, it leads to a reduction in the density of the steel; the combination of Al and Si at the concentrations used typically reduces the overall density from some $7.8\,\mathrm{g\,cm^{-3}}$ to about $7.3\,\mathrm{g\,cm^{-3}}$.

The alloys have a rather low yield strength at 200-300 $\mathrm{MN\,m^{-2}}$ but the ultimate tensile strength can be much higher, in excess of $1100\,\mathrm{MN\,m^{-2}}$. This is because the strain-hardening coefficient is large, resulting in a great deal of uniform elongation, and a total elongation of some 60-95%. The effect of mechanical twinning is two-fold. The twins add to plasticity, but they also have a powerful effect

in increasing the work-hardening rate by subdividing the untwinned austenite into finer regions (Fig. 44).

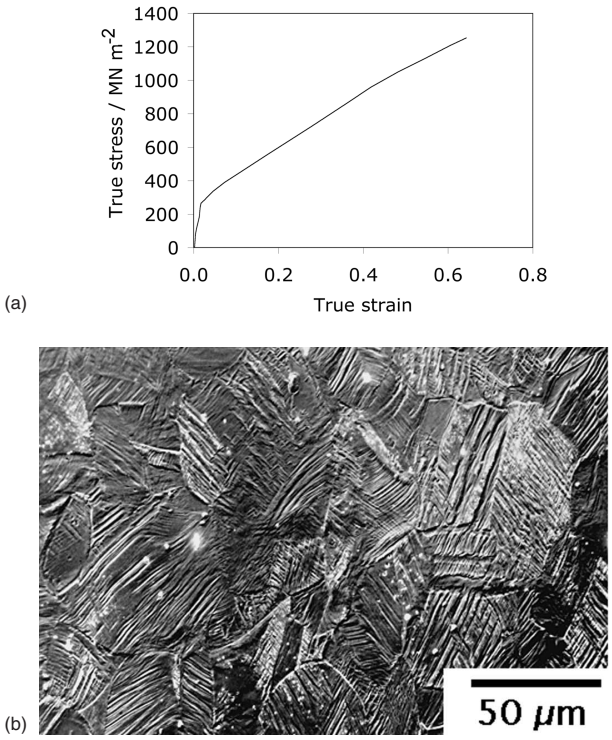

FIGURE 44. (a) Typical stress-strain curve for a TWIP steel. (b) Optical microstructure of a TWIP steel following deformation, showing profuse twinning (image and data courtesy of Frommeyer, G., Brüx, U. and Neumann, P).

One major advantage of TWIP steels is that they are austenitic and they maintain attractive properties at cryogenic temperatures ($-150°C$) and high strain rates, e.g., $10^3\,s^{-1}$. They therefore have great potential in enhancing the safety of automobiles by absorbing energy during crashes.

10. Mitigation of Residual Stress

Residual stress is that which remains in a body which is stationary and at equilibrium with its surroundings. It can be very detrimental to the performance of a material or the life of a component.

Jones and Alberry conducted an elegant series of experiments to illustrate the role of transformations on the development of residual stress in steels. Using bainitic, martensitic and stable austenitic steels, they demonstrated that transformation plasticity during the cooling of a uniaxially constrained sample from the austenite phase field, acts to relieve the build up of thermal stress as the sample cools. By contrast, the non-transforming austenitic steel exhibited a monotonic increase in residual stress with decreasing temperature, as might be expected from the thermal contraction of a constrained sample. When the steels transformed to bainite or martensite, the transformation strain compensated for any thermal contraction strains that arose during cooling. Significant residual stresses were therefore found to build up only after transformation was completed, and the specimens approached ambient temperature (Fig. 45).

The experiments contain other revealing features. The thermal expansion coefficient of austenite ($1.8 \times 10^{-6}\,\mathrm{K}^{-1}$) is much larger than that of ferrite ($1.18 \times 10^{-6}\,\mathrm{K}^{-1}$), and yet, the slope of the line prior to transformation is smaller when compared with that after transformation is completed (Fig. 45). This is because the austenite deforms plastically; its yield strength at high temperatures is reduced so much that the sample is unable to accommodate the contraction strains elastically. Thus, the high temperature austenite part of each curve is virtually a plot of the yield strength as a function of temperature, as is evident from the comparison versus the actual yield strength data also plotted on Fig. 45a.

In the region of the stress/temperature curve where transformation happens, the interpretation of experimental data of the kind illustrated in Fig. 45 is difficult. In the case of displacive transformations, the shape change due to transformation has a shear component which is much larger than the dilatational term. This will give rise to significant intergranular microstresses, part of which will be relaxed plastically. This shear component will on average cancel out in a fine grained polycrystalline sample containing plates in many orientations so that the average type II microstress component will be zero. However, the very nature of the stress effect is to favour the formation of selected variants], in which case the shear component rapidly begins to dominate the transformation plasticity. Fig. 45a shows that the stress can temporarily change sign as the sample cools. This is because the stress selected variants continue to grow preferentially until transformation is exhausted.

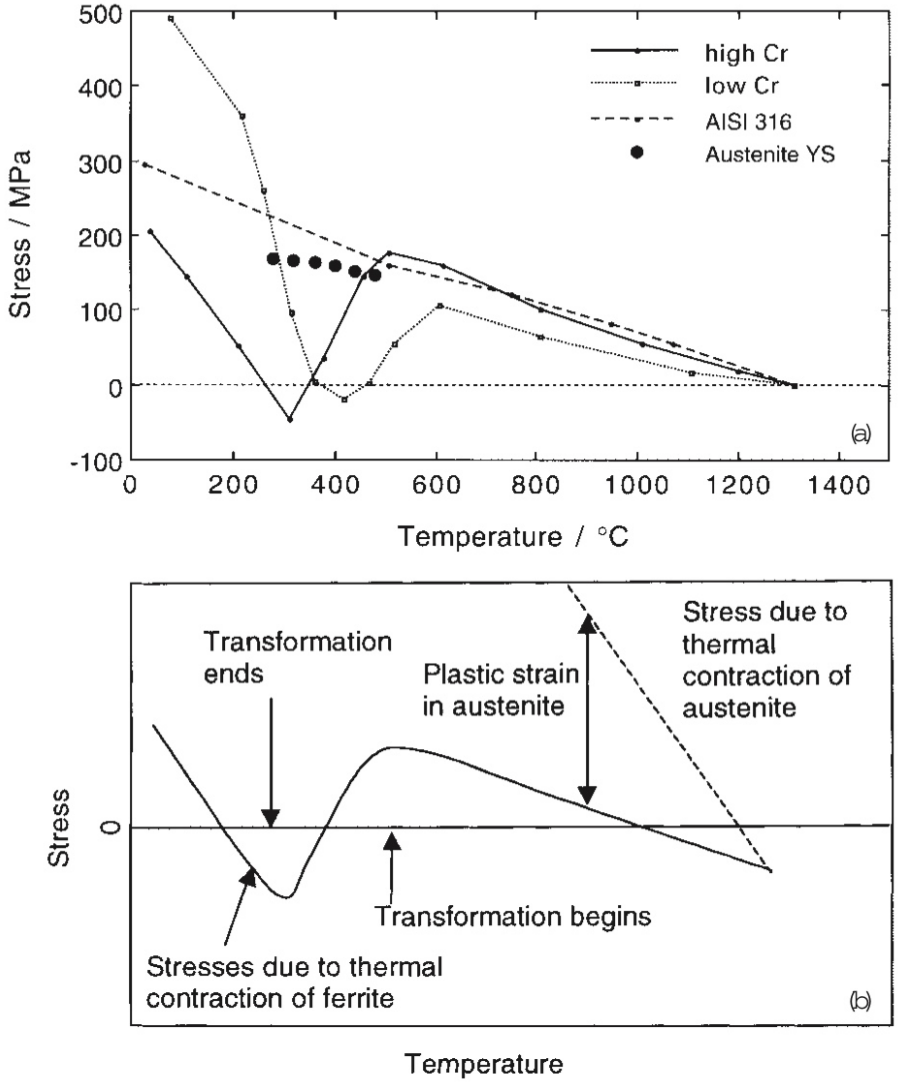

FIGURE 45. (a) The axial macro stress that develops in uniaxially constrained samples during cooling of a martensitic (9Cr1Mo), bainitic ($2\frac{1}{2}$Cr1Mo) and austenitic steel (AISI 316). Also plotted are some experimental data for the yield strength of austenite in a low-alloy steel. (b) Interpretation of the Alberry and Jones experiments. The thermal expansion coefficient of austenite is much larger than that of ferrite.

Notice that if transformation is completed at a higher temperature, then the ultimate level of stress at ambient temperature is larger, since the fully ferritic sample contracts over a larger temperature range. To reduce the residual stress level at ambient temperature requires the design of alloys with low transformation temperatures. The sort of high strength welding alloys used for making submarine hulls tend to have very low transformation temperatures ($< 250°C$). This fact may be fortuitous, but such alloys should be less susceptible to cracking induced by the development of macro residual stresses. Fig. 46 illustrates one kind of distortion found in welds, measured in terms of the angle θ through which the unconstrained plates rotate during the cooling to ambient temperature. It has now been demonstrated that the use of appropriate martensitic weld metal can dramatically reduce the distortion.

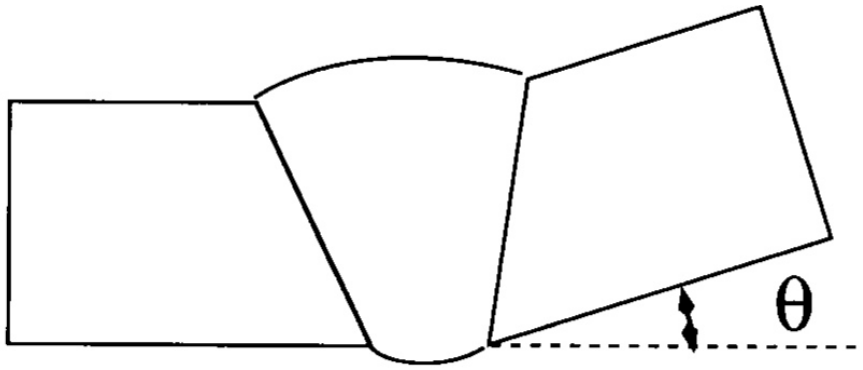

FIGURE 46. An illustration of the distortion caused when a pair of coplanar plates are welded together and the joint is then allowed to cool to ambient temperature.

11. Bulk Nanostructured Steel

A nanostructured material is here defined as one containing an exceptionally large density of strong interfaces, rather than one which simply contains a minor fraction of features such as precipitates, which are small in size. The desire for such materials in the engineering context comes from the expectation of novel mechanical properties, particularly the stress that can safely be tolerated in service. It is difficult to invent such materials because any design must address three basic issues:

(i): it should ideally be possible to make samples which are large in all dimensions, not simply wires or thin sheets;

(ii): there are commercially available steels in which the distance between interfaces is of the order of 250–100 nm. The novelty is in approaching a structural scale in polycrystalline metals which is an order of magnitude smaller.

(iii): The material concerned must be cheap to produce if it is not to be limited to niche applications. A good standard for an affordable material is that its cost must be similar to that of bottled water when considering weight or volume.

These are formidable challenges and the process of design can begin with a consideration of how strength can be achieved. The long–range periodicity which is assumed to typify the crystalline state is in practice punctuated by defects, some of which make a significant contribution to configurational entropy and hence can exist in thermodynamic equilibrium. This kind of entropy scales with the number of entities (atoms) in the crystal and hence it is only possible to approximate perfection in small crystals. Such crystals can be strong because in the absence of defects, deformation must occur by the wholesale glide of planes over each other, rather than by the propagation of discontinuities such as dislocations. Micrometer sized crystals of pure iron have achieved strength levels in excess of 10 GPa, although in principle the strength can exceed 20 GPa. The crystals becomes weaker as they are made larger, both because of the thermodynamically stabilised defects and also accidents of growth. This is fundamentally why the impressive mechanical properties of carbon *nanotubes* are not maintained (and indeed, should not be expected to be maintained) when the tubes become long.

An alternative method for manufacturing sizeable strong materials is to introduce large numbers of defects such as interfaces or dislocations, which interfere with the ordinary mechanisms of slip or twinning. The defects can be introduced by deformation. Techniques which involve severe plastic deformation are limited in the shape of the final product and in the quantity that can be produced at reasonable cost.

Examples include fine nanostructured–wire with a strength in excess of 5 GPa; metals subjected to equal–channel angular extrusion in which redundant work is used in order to achieve large plastic strains whilst maintaining the external shape of the object being deformed. Accumulative roll–bonding involves the repeated rolling and folding of sheet material in order to accomplish strain increments without thinning the sample entering the rolls; the process is suited for large scale production but does not lead to particularly fine grains, which tend to be closer to micrometers than nanometers in size.

Thermomechanical processing is particularly suited to the large scale production of fine–grained steels by phase transformation from the deformed parent austenite. However, the minimum ferrite grain size achieved in practice is about $1\,\mu$m, partly because the speed of production and the thickness of the steel leads to recalescence during transformation, and hence prevents the achievement of the large undercoolings needed to refine the grain size.

There are a couple of further difficulties. The ductility decreases sharply as the grain size in a polycrystalline metal is reduced. Secondly, there is often a requirement for rapid heat–treatment which becomes impractical for large components.

A recent development seems to avoid all of these difficulties, and meets the criteria outlined in the opening paragraph of this chapter. A nanostructure has been achieved in large lumps of steel by phase transformation, with the design of the steel based on an understanding of the atomic mechanisms of crystal growth in the solid state.

11.1. **Alloy design.** Suppose we now use theory to estimate the lowest temperature at which bainite can form. Such calculations are illustrated in Fig. 47a, which shows for an example steel, how the B_S and M_S temperatures vary as a function of the carbon concentration. There appears to be no lower limit to the temperature at which bainite can be generated. On the other hand, the rate at which bainite forms slows down dramatically as the transformation temperature is reduced, Fig. 47b. It may take hundreds or thousands of years to generate bainite at room temperature. For practical purposes, a transformation time of tens of days is reasonable, corresponding to a carbon concentration of about 1 wt%, in which case bainite can be generated at a temperature as low as 125°C, which is so low that the diffusion distance of an iron atom is an inconceivable 10^{-17} m over the time scale of the experiment!

A steel designed on this basis was manufactured and characterised; Fig. 48 shows the structure obtained following isothermal transformation at 200°C, consisting of platelets of bainitic ferrite only 200–400 Å thick, with intervening regions of the parent austenite (γ). This *retained* austenite is important because when it undergoes stress or strain–induced martensitic transformation, it enhances the work–hardening

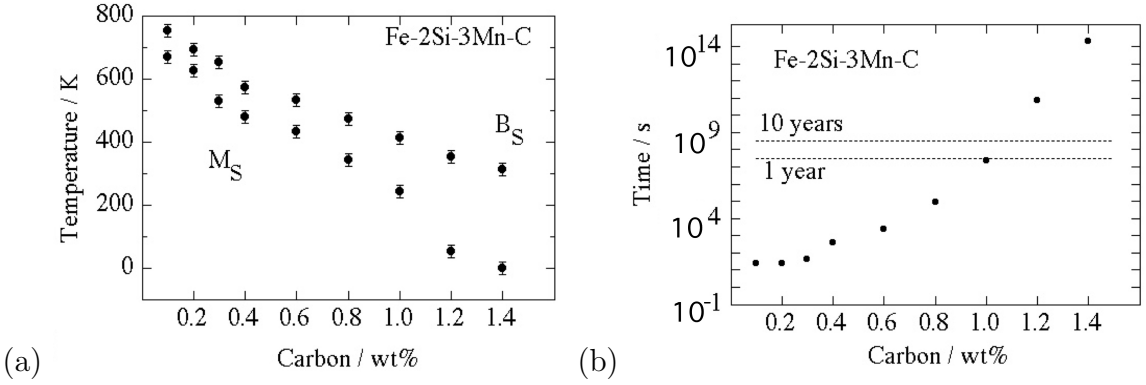

FIGURE 47. (a) Calculated transformation start temperatures in Fe-2Si-3Mn steel as a function of the carbon concentration. (b) The calculated time required to initiate bainite.

capacity of the material, thereby avoiding the usual problem of fine–grained metals where ductility diminishes as the grain size is reduced.

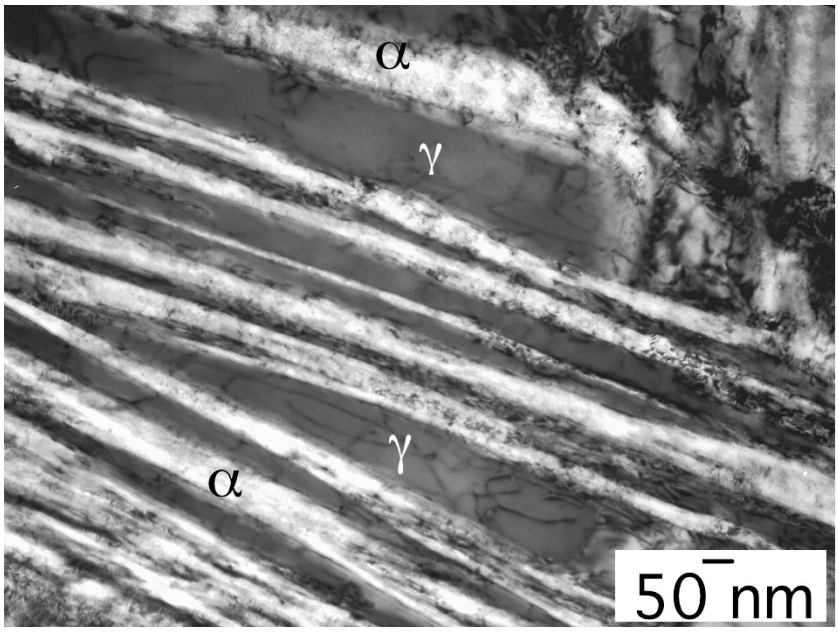

FIGURE 48. Fe-0.98C-1.46Si-1.89Mn-0.26Mo-1.26Cr-0.09V wt%, transformed at 200°C for 15 days. Transmission electron micrograph.

The bainite obtained by low–temperature transformation is harder than ever achieved, with values in excess of 700 HV. Some strength, ductility and toughness data are

illustrated in Fig. 49. The simple heat treatment involves the austenitisation of a chunk of steel (at say 950°C), followed by a gentle transfer into an oven at the low temperature (say 200°C) to be held there for ten days or so. There is no rapid cooling – residual stresses are avoided. The size of the sample can be large because the time taken to reach 200°C from the austenitisation temperature is much less than that required to initiate bainite. This is an important commercial advantage.

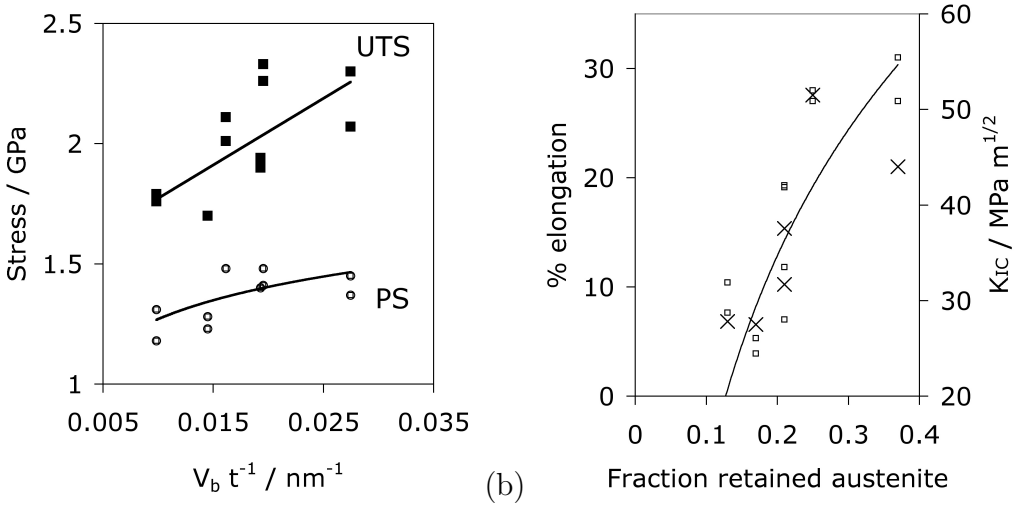

FIGURE 49. Some mechanical properties of two superbainitic steels. (a) The ultimate tensile strength (UTS) and 0.2% proof strength as a function of the volume fraction of bainitic ferrite (V_b) divided by the ferrite platelet thickness t. (b) Ductility (points and curve) and toughness K_{IC} represented as crosses.

12. Question Sheet

Please use this question sheet as a supplement to the on-line edX sets.

12.1. **Martensite.**

a. Give two examples of deformations that change the crystal structure and two examples of those which do not. [20%]

b. A simple shear can transform the Cubic F structure of austenite into the hexagonal close-packed ε martensite. This consists of a displacement of $\frac{a}{6}\langle 112\rangle$ on successive close-packed planes. Calculate the shear strain associated with the transformation. (a is the lattice parameter of austenite). [20%]

c. How many different crystallographic variants of ε-martensite can in principle form within a single austenite grain? [20%]

d. Fig. 50 shows a stereographic projection of austenite showing the ε habit planes of the form $\{111\}$ and shear directions of the form $\langle 112\rangle$. Which is the most favoured crystallographic variant that is stimulated to grow by applying a tensile stress along the direction [123]? [30%]

e. Which alloying element promotes the hexagonal close-packed form of iron, and hence ε-iron, under ambient conditions? [10%].

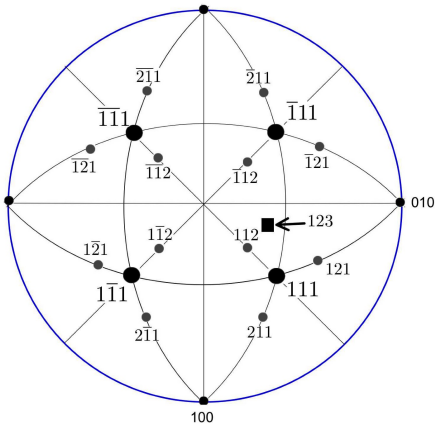

Figure 50. Stereographic projection of austenite, showing also the location of the tensile axis along [123].

12.2. **Bainite and Martensite.**

a. Describe an experiment that can establish whether or not carbon diffuses during the growth of bainite. [20%]

b. A particular steel has the chemical composition Fe-0.2C-2Si-2Mn wt%, the T_0 curve of which is presented below. Beginning with the fully austenitic state, it is transformed isothermally to bainite at 400°C until the reaction stops. Calculate the volume fractions of the phases present, and the carbon concentration of the austenite when the reaction ceases. Comment on the role of the silicon and state any assumptions involved in your calculation. [30%]

c. Describe what might happen when the mixture of phases generated by the experiment above is cooled to ambient temperature. [10%].

d. In a second experiment, the steel is heated into the fully austenitic state until the austenite grain size reaches 40 μm. It is then quenched to produce martensite. If the free energy change accompanying martensitic transformation is 1000 J mol^{-1}, and the shear and dilatational components of the shape deformation are $s = 0.26$ and $\delta = 0.03$, calculate the maximum thickness of the martensite plates that form. [25%]

e. Explain how the thickness of the bainite plates produced in (b) might compare against the calculated thickness of the martensite plates. [15%]

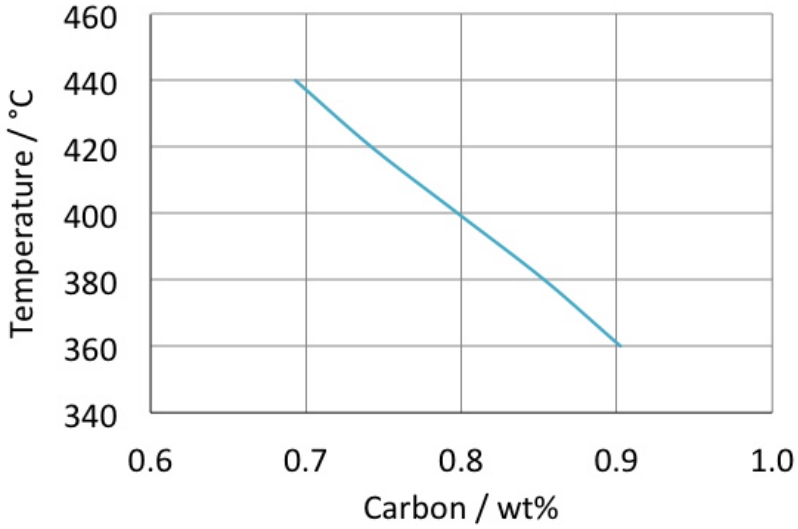

[The strain energy per unit volume of an elastically accommodated plate of martensite is $\frac{c}{r}\mu(s^2+\delta^2)$, where $\mu = 80\,\mathrm{GPa}$ is the shear modulus of the austenite, and $\frac{c}{r}$ is the thickness to length ratio of the martensite plate. The molar volume of iron is about $7\times10^{-6}\,\mathrm{m^3\,mol^{-1}}$.]

12.3. **Ferrite.**

a. The data given in the table below describe how the thickness of an allotriomorph of ferrite varies with time (t) during the isothermal transformation of austenite of grain size 20 μm. Plot the data, both as a function of t and $\sqrt{t}$. Explain the form of the relationship between the thickness of the ferrite and the transformation time. [30%]

Thickness of α layer / μm	Time / s
0	0
0.47	2
0.64	4
0.90	8
1.28	16

b. Describe what is meant by *hard impingement* and *soft impingement*. [10%]

c. Illustrate the distribution of solute ahead of the transformation interface, marking on your diagrams the equilibrium compositions of the parent (γ) and product (α) phases ($c^{\gamma\alpha}$ and $c^{\alpha\gamma}$ respectively) and the average composition $\overline{c}$. How would you expect the concentration profile to change as the thickness of the ferrite layer becomes a substantial proportion of the austenite grain size? [30%]

d. In a ternary steel containing both manganese and carbon as solutes, the austenite is transformed isothermally into allotriomorphic under paraequilibrium conditions. Sketch an isothermal section of the iron-rich part of the Fe-Mn-C paraquilibrium diagram, indicating tie-lines within the $\alpha + \gamma$ phase field. Draw on this diagram the equilibrium $\alpha + \gamma$ phase field together will illustrative tie-lines. By comparing the equilibrium and paraequilibrium ties lines, indicate the solute that is trapped as ferrite grows. Explain why the phase boundaries of these two diagrams meet when the Mn concentration is zero. [30%]

12.4. **Ferrite, TRIP, Bainite.**

a. Why does the common tangent construction, on plots of the free energy versus composition curves in a binary system, lead to the equilibrium compositions of the phases where the tangent touches the curves simultaneously? At a constant temperature, the equilibrium compositions in a binary system are connected by a unique tie-line. Why is the tie-line no longer unique in the ternary case? [30%]

b. What is meant by *paraequilibrium* in the context of an Fe-Mn-C steel? Comment on how the concentration of the solutes would be expected to vary across the ferrite-austenite interface during paraequilibrium growth, assuming that you can measure the composition with atomic resolution. [20%]

c. Explain qualitatively why the strain caused by deformation-induced martensitic transformation in TRIP-assisted steel cannot explain the remarkably ductility observed in spite of the high-strength of these alloys. What then is the cause of this useful combination of strength and ductility? [20%]

d. Describe four conditions necessary to facilitate the production of tonnage quantities of nanostructured steel. Given an interfacial energy per unit area of $0.2\,\mathrm{J\,m^{-2}}$, estimate the energy stored in a material where the interfaces are spaced 20 nm apart. [30%]

12.5. **Pearlite.**

a. Why does pearlite in an Fe-C alloy grow at a constant rate, whereas the rate of growth of allotriomorphic ferrite decreases as the ferrite thickens? [10%]

b. Derive an expression relating the interlamellar spacing S, and the amount of ferrite (α)-cementite (θ) and the interfacial area per unit volume S_V. What is the free energy consumed in creating these interfaces, as a function of S? If the chemical free energy change available for transformation is $2.86 \times 10^7\,\mathrm{J\,m^{-3}}$, and the α/θ interfacial energy per unit area is $0.6\,\mathrm{J\,m^{-2}}$, find the critical interlamellar spacing S_C whence all the driving force is consumed in creating the interfaces. [30%]

c. Show therefore, that the driving force available for transformation (ΔG) after accounting for the α/θ interfacial energy, can be expressed as $\Delta G \propto (1 - [S_C/S])$. [10%]

d. How does the gradient of concentration at the transformation front vary with the interlamellar spacing? Assuming that the growth velocity is proportional to ΔG, and to the gradient, show that the maximum in growth rate occurs when $S = 2S_C$. [30%]

e. Explain the microstructural features of pearlite that control (a) its strength and (b) its toughness. [20%]

References

[1] J. W. Christian. *Theory of Transformations in Metals and Alloys, Part I.* Pergamon Press, Oxford, U. K., 2 edition, 1975.

[2] H. K. D. H. Bhadeshia. Critical assessment: Diffusion-controlled growth of ferrite plates in plain carbon steels. *Materials Science and Technology*, 1:497–504, 1985.

[3] W. W. Gerberich, G. Thomas, E. R. Parker, and V. F. Zackay. Metastable austenites: decomposition and strength. In *Second International Conference on Strength of Metals and Alloys*, pages 894–899, Ohio, USA, 1970. ASM International.

[4] J. R. Patel and M. Cohen. Criterion for the action of applied stress in the martensitic transformation. *Acta Metallurgica*, 1:531–538, 1953.

[5] H. K. D. H. Bhadeshia. TRIP-assisted steels? *ISIJ International*, 42:1059–1060, 2002.

[6] P. J. Jacques. Transformation-induced plasticity for high strength formable steels. *Current Opinion in Solid State and Materials Science*, 8:259–265, 2004.

[7] S. Chatterjee, M. Murugananth, and H. K. D. H. Bhadeshia. δ-TRIP steel. *Materials Science and Technology*, 23:819–827, 2007.

[8] H. L. Yi, K. Y. Lee, and H. K. D. H. Bhadeshia. Extraordinary ductility in Al-bearing δ-TRIP steel. *Proceedings of the Royal Society A*, 467:234–243, 2011.